

**Mapping playa evaporite minerals and associated sediments in Death Valley,
California, with multispectral thermal-infrared images**

by

James K. Crowley¹

and

Simon J. Hook²

¹ U. S. Geological Survey

Mail Stop 927

Reston, Virginia 22092

jcrowley@bgrdg1.er.usgs.gov

Tel, (703) 648-6356

FAX (703) 648-4828

² Jet Propulsion Laboratory

4800 Oak Grove Drive

Pasadena, California 91109

simon@lithos.jpl.nasa.gov

Tel. (81 8) 354-0974

FAX (818) 354-0966

Abstract

Efflorescent salt crusts and associated sediments in Death Valley, California, were studied with remote-sensing data acquired by the NASA thermal-infrared multispectral scanner (TOMS). Nine spectral classes that represent a variety of surface materials were distinguished, including several classes that reflect important aspects of the playa ground-water chemistry and hydrology. Evaporite crusts containing abundant thenardite (sodium sulfate) were mapped along the northern and eastern margins of the Cottonball Basin--areas where the inflow waters are rich in sodium. Gypsum (calcium sulfate) crusts were more common in the Badwater Basin, particularly near springs associated with calcic ground waters along the western basin margin. Evaporite-rich crusts generally marked areas where ground water is periodically near the surface, and thus, able to replenish the crusts through capillary evaporation. Detrital silicate minerals were prevalent in other parts of the salt pan where shallow ground water does not affect the surface composition. The surface features in Death Valley change in response to climatic variations on several different time scales. For example, salt crusts on low-lying mudflats form and redissolve during seasonal-to-interannual cycles of wetting and desiccation. In contrast, recent flooding and erosion of rough-salt surfaces in Death Valley probably reflects increased regional precipitation spanning several decades. Remote-sensing observations of playas can provide a means for monitoring changes in evaporite facies and for better understanding the associated climatic processes. At present such studies are limited by the availability of suitable airborne scanner data. However, with the launch of the Earth Observing System (EOS) AM-1 Platform in 1998, multispectral visible/near-infrared and thermal-infrared remote sensing data will become globally available.

Introduction

Playa evaporite deposits like those of Death Valley, California, are common features in desert regions where closed drainage basins and high evaporation rates favor the development of brines and saline minerals. Local variations in rock type and weathering produce a wide chemical range in brine and mineral compositions (Eugster, 1980), and some playas contain economic mineral resources, including boron- or lithium-rich brines (Vine, 1976; Reeves, 1978). In addition to their possible economic value, playa evaporates may serve as indicators of short-term climate variations. Efflorescent salt crusts, produced by the capillary evaporation of near-surface brines, typically cover many square kilometers in playa settings (Eugster and Hardie, 1978). The salt crusts are delicate sedimentary features, affected by seasonal-to-interannual changes in rainfall, inflow water volume, temperature, and wind ablation (Smoot and Lowenstein, 1991; Smith and others, 1987). Observing the response of playa efflorescent crusts to climate-driven variations in these parameters has been suggested as an approach for monitoring climate changes in arid regions (Crowley, 1993). However, the ability to study salt crusts is hampered by their large areal extent, and in many parts of the world, by difficult access.

Remote-sensing techniques are an important tool for playa studies. Multispectral images have strong potential for use in mapping efflorescent salts that exhibit short-wave infrared (1.0-2.5 μm) and thermal-infrared (8.0-12.0 μm) spectral absorption features related to hydrogen-bonded water molecules, and to hydroxyl, carbonate, sulfate, and borate anion groups (Farmer, 1974; Crowley, 1991; Salisbury et al., 1991). Short-wave infrared spectra are also very sensitive to minor hydrate mineral components of natural salt mixtures and to moisture variations across playa surfaces (Crowley, 1993). Based on the spectral detection of certain minerals that serve as chemical indicators, it is also possible in some

cases to infer the compositional type of the parent brine that an evaporite sample represents (Crowley, 1993).

Previous work in Death Valley, California, has demonstrated the utility of NASA's Airborne Visible/Infrared Imaging Spectrometer (AVIRIS) for mapping playa evaporite minerals based on their short-wave infrared spectral proportion (Crowley, 1993). However, in that study it was noted that several chemically important evaporite minerals, including thenardite (Na_2SO_4) and anhydrite (CaSO_4), which lack short-wave infrared spectral features, could not be detected with data from the AVIRIS sensor. These anhydrous sulfate minerals do exhibit spectral features in the thermal-infrared wavelength range, and thermal-infrared remote sensing data may provide a useful complement to short-wave infrared data for mapping evaporites. This potential application is explored using imagery acquired by NASA's Thermal Infrared Multispectral Scanner (TIMS), a six-channel airborne instrument operating in the 8-12 μm wavelength region (Palluconi and Meeks, 1985). The study is part of an ongoing project to investigate the use of remotely-sensed data in multiple wavelength regions for observing playa evaporates.

Theoretical Framework

A wide variety of minerals exhibit diagnostic spectral features in the thermal-infrared wavelength range. The major emissivity features of rock-forming silicates are mainly due to fundamental vibration modes of the SiO_4 anion group (Hunt, 1980). In evaporates, emissivity features generally result from sulfate, borate, and carbonate anion groups (Hunt and Salisbury, 1971; Hunt et al., 1971; 1972; Hunt, 1980). Anhydrous chloride minerals, including halite (NaCl) and sylvite (KCl), are spectrally featureless in the thermal-infrared wavelength region, although, as discussed in a later section, minor sulfate and other impurities may be evident in emissivity spectra of natural salt crusts that are chloride-rich.

Figure 1A illustrates calculated emissivity spectra for a number of pure evaporite minerals, and also depicts the same spectra after convolution to the six TIMS filter functions. The six sulfate minerals included in the figure (thenardite, gypsum, anhydrite, hexahydrate ($\text{MgSO}_4 \cdot 6\text{H}_2\text{O}$), bloedite ($\text{Na}_2\text{Mg}(\text{SO}_4)_2 \cdot 4\text{H}_2\text{O}$), and glauberite ($\text{Na}_2\text{Ca}(\text{SO}_4)_2$), exhibit spectral differences related to SO_4 anion site distortions in each mineral structure (see Ross, 1974). In principle, these distinctive spectral features might permit the minerals to be identified with thermal-infrared remote-sensing data. In practice, however, the sulfate minerals seldom occur in pure form, and particle size, surface moisture variations, and other complex factors must be considered in remote-sensing spectral interpretations (Eastes, 1989; Salisbury and others, 1991). The ulexite ($\text{NaCaB}_5\text{O}_6(\text{OH})_6 \cdot 5\text{H}_2\text{O}$) spectrum is typical of borate minerals in that there are several emission features in the 8-12 μm wavelength range. Unfortunately, when most borate emission spectra are convolved to the six TIMS filter functions the spectral features are undersampled and become obscured. Similarly, the spectrum for the carbonate mineral, trona ($\text{Na}_3(\text{CO}_3)(\text{HCO}_3) \cdot 2\text{H}_2\text{O}$), exhibits a single narrow feature near 11.7 μm , and the corresponding TIMS spectrum lacks useful shape information.

Figure 1B shows calculated emissivity spectra for several pure silicate minerals that are common in Death Valley as well as other playa settings. All of the emissivity features displayed between approximately 8.0-10.0 μm result from Si-O stretching vibration modes (Farmer, 1974; Hunt, 1980). Phyllosilicate minerals also can exhibit emissivity features in the 10.0 -12.5 μm wavelength region associated with bonding modes involving Mg-OH and Al-OH. However, none of the phyllosilicate spectra included in Figure 1B show these features. Table 1 lists the locality and/or source of each evaporite and silicate reference sample.

The occurrence of various evaporite minerals in playas is closely linked to the chemical composition of local ground waters. In fact, evaporite mineral formation

plays an important role in the chemical evolution of playa ground waters and brines through the action of chemical divides. For example, the early precipitation of calcite (CaCO_3), with accompanying removal of calcium and carbonate ions in equal proportions, causes water compositions to branch into one of two broad chemical types: Waters with initial ion concentrations of $\text{Ca}^{+2}/(\text{HCO}_3^- + \text{CO}_3^{2-})$ greater than 1 commonly pass through a second chemical divide involving gypsum and develop into neutral Na- SO_4 -Cl brines; waters with initial $\text{Ca}^{+2}/(\text{HCO}_3^- + \text{CO}_3^{2-})$ less than 1 typically evolve into alkaline Na- HCO_3 -Cl brines (Eugster and Hardie, 1978). Several other permutations in brine composition are possible, but the general course towards neutral or alkaline compositions is fixed at the calcite precipitation stage (Eugster, 1980). The minerals associated with major chemical divides, including calcite, dolomite, and gypsum, are ubiquitous in playa settings. Other minerals are found only in association with brines of a particular chemical composition. For example, brines that are rich in sodium and bicarbonate typically produce efflorescent salt crusts that contain abundant trona. Magnesium- and sulfate-rich brines produce hexahydrite and/or bloedite. Eugster (1980) and Eugster and Hardie (1978) discuss chemical divides, other fractionation mechanisms, and mineral assemblages that are characteristic of different brine types.

Study Area

Death Valley lies at the western margin of the Basin and Range physiographic province and contains a variety of rock types (Hunt and Mabey, 1966). The oldest rock units are Precambrian schist and gneiss, which compose much of the Black Mountain Range along the southeastern valley margin, as well as portions of the Panamint Range to the west (fig. 2). Overlying these rocks are metasediments, including quartzite, metaconglomerate, argillite, and dolomite, which compose much of the Panamint Range. A thick sequence of Paleozoic sedimentary rocks, consisting mostly of carbonates, is exposed on the eastern slope of the Panamint Range. At the north end of the Black Mountains is the Tertiary Artist Drive Formation, composed mainly of felsic volcanic rocks and interbedded elastic sedimentary rocks. Unconformably overlying the Artist Drive Formation is the Furnace Creek Formation of Miocene and Pliocene(?) age. The Furnace Creek Formation is a mixture of conglomerate, saliferous playa sediments, and interbedded basalts and tuffs (McAllister, 1970; 1976). This formation hosts large borate mineral deposits that have been exploited since the early twentieth century (Barker and Wilson, 1975; Smith, 1985). The Furnace Creek Formation is unconformably overlain by the Funeral Formation of Pliocene and Pleistocene(?) age (McAllister, 1970). The Funeral Formation consists mainly of poorly-stratified conglomerate, sandy mudstone, and basaltic flows. Additional details of the structure and stratigraphy of the Death Valley region and the Furnace Creek borate deposits are in Hunt and Mabey (1966), McAllister (1970; 1976), and Barker and Barker (1985).

The Death Valley salt pan covers over 500 km² and contains surface crusts of evaporite minerals ranging from a few millimeters to more than one meter in thickness. As discussed by Hunt and others (1966), the salt pan displays a zoned arrangement of evaporite minerals, including a central chloride zone, surrounded by

fringing zones of sulfate and carbonate salts. This zonation reflects differences in the solubilities of the salts, with more soluble minerals generally forming towards the center of the salt pan. Beneath the surficial deposits alternating layers of salt and clay-rich sediment have been found to depths of more than 300 m.

This report focuses on two subareas of the Death Valley salt pan, the Cottonball Basin and the Badwater Basin, which exhibit mineralogical variations related to differences in the surrounding rock types and hydrological regimes. The Cottonball Basin at the north end of the salt pan receives most of its inflow as ground water, a significant fraction of which is derived from, or at least flows through, the Furnace Creek and the Funeral Formations. This inflow has somewhat greater Na/Ca values than inflow to other parts of the salt pan, and is locally higher in bicarbonate (Hunt and others, 1966). The Badwater Basin in the southern part of the salt pan receives ground-water inflow derived from Paleozoic sediments (mainly carbonates) located on the eastern slopes of the Panamint Range, as well as from the metamorphic rocks of the Black Mountains. The Badwater Basin also receives sporadic, but volumetrically important, surface-water inflow from the Amargosa River, which enters the valley from the south. The Badwater Basin inflow sources generally have lower Na/Ca values and are less bicarbonate-rich than the inflow to the Cottonball Basin (Hunt and others, 1966).

Data Collection and Analysis

TIMS data consist of imagery recorded in six spectral channels that are designed to take advantage of an atmospheric window extending from about 8.0-14.0 μm . The data used in this study were acquired from an altitude of approximately 9,000 m by the NASA-Ames C-130 aircraft at 11:00 AM, April 6, 1994. The wavelengths of the six TIMS bandpasses vary slightly from year to year and in this case had band centers at 8,412, 8,791, 9,199, 9,893, 10,743, and 11,641 μm . TIMS has an instantaneous field of view of 2.5 mrad and a total field of view of 76.560. The swath width varies with the altitude of operation and for this flight was approximately 11 km, with each image pixel corresponding to a ground spot of about 20 x 20 m. Additional information on the TIMS instrument design and operation is given in Palluconi and Meeks (1985) and Realmuto and others (1995a; 1995b).

At the time these TIMS data were collected, the Death Valley basin floor was generally dry, although the lowest areas of the salt pan had moisture present just below a thin (1-2 cm) surface layer of dry salt. Heavy regional rainfall and flooding of some areas of the salt pan in January, 1993, was followed by sparse rainfall (< 10 mm) over the next 22 months. While such aridity is not unusual for Death Valley, the efflorescent salt crusts of the basin floor were perhaps better developed at the time of this data set than at any other time during the preceding seven years (J. Crowley, pers. obs.). This TIMS data set therefore holds particular interest for the relatively dry surface condition that it represents.

A total of approximately 100 field samples were collected in December 1993, April 1994, and December 1994. Directional-hemispherical thermal-infrared reflectance spectra of the samples were measured in the laboratory using a Nicolet 5DXB FTIR spectrometer, and were subsequently converted to emissivity by using Kirchhoff's Law (Salisbury and others, 1991; 1994). The samples were analyzed

by X-ray powder diffraction (XRD) to determine mineralogy. Sample mineralogy and other information is given in Table 1.

In addition to the laboratory spectra, *in situ* spectral measurements were made at the majority of sample sites by using the JPL field emission spectrometer (μ FTIR) developed by Designs and Prototypes, Inc. The μ FTIR is a lightweight, field-portable interferometer with a spectral resolution of approximately 6 cm^{-1} . Calibration of the instrument is achieved using a portable blackbody and the data are recorded directly to a portable computer. Some of the μ FTIR data have an erratic saw-tooth appearance due to a calibration error in the downwelling radiance measurement (A. R. Korb and others, Portable FTIR spectroradiometer for field measurements of radiance and emissivity, submitted to Applied Optics). In the present study, the calibration error was most noticeable in samples having low emissivity in the $10\text{-}12\text{ }\mu\text{m}$ wavelength region (see Figure 6). Additional description of the μ FTIR instrument, its operation, and examples of other spectra can be found in Hook and Kahle (in press).

The TIMS sensor measures the energy radiated from the Earth's surface and modified by the atmosphere. Initially, the TIMS data were calibrated to radiance at the sensor (Palluconi and Meeks, 1985) and then the atmospheric component of the total radiance was removed by using the MODTRAN radiative transfer model (Berk and others, 1989). MODTRAN derives values for the atmospheric correction based on an input atmospheric profile. Default parameters for this profile are available within MODTRAN, or the parameters can be obtained through direct atmospheric measurements at the time of the aircraft overflight. In this study no direct atmospheric measurements were available and the default mid-latitude winter profile was used. The winter profile, rather than the summer profile, was chosen because the latter contains far more atmospheric moisture than would be expected for a desert area. An alternative approach would have been to use a

mid-latitude summer temperature profile with a mid-latitude winter moisture profile. Following the initial atmospheric correction, the brightness temperatures of two areas, one of rough-salt and another covered by vegetation, were examined. The rough-salt area consisted mainly of dry halite with small amounts of entrained clay and silt. Such areas have an unusual microtopography of pits and spires with relief on the order of 0.2-0.5 m. Although some samples collected from the rough-salt exhibited spectral features when measured at close range (e.g. in the laboratory), virtually all of the rough-salt areas exhibited very low spectral contrast in the remotely sensed data. The rough surface evidently behaves as a cavity radiator--simulating an almost perfect blackbody. Similarly, vegetation has a near-constant emissivity at the spectral resolution of the TIMS and may also be regarded as an approximate blackbody (Salisbury and D'Aria, 1992). Brightness temperatures in each of the six TIMS channels should therefore be approximately constant over these two types of targets (although brightness temperatures will vary between targets). After the initial calibration using the default mid-latitude winter profile, the brightness temperature values in channel one were observed to be considerably greater than those in the other channels. Accordingly, the amount of water vapor in the profile was reduced until there was good agreement between the temperature values in all six TIMS channels for the two types of calibration targets. Although this required a 70 percent reduction in the original water vapor profile value, it should be noted that there was so little water in the initial profile that the resulting changes to the radiance spectra were very minor. Furthermore, the alpha-residual technique used to extract emissivity information from the TIMS radiance data (see below), is relatively insensitive to small errors in surface temperature, which might be caused by errors in the atmospheric correction. This approach to atmospheric correction of TIMS data is discussed further by Hook and others (1992).

After the atmospheric correction, the ground radiance values are a function only of surface temperature and emissivity. In this study we were interested primarily in emissivity variations that relate to variations in evaporite mineralogy. This emissivity information was extracted with the alpha-residual technique discussed by Hook and others (1992) and Kealy and Hook (1993). The technique linearizes (by taking logarithms) Wien's approximation of the Planck function relating radiance to temperature and emissivity. The linear equation is manipulated to isolate and remove a constant temperature term for each spectral band to produce a temperature-independent index. The resulting alpha-residual spectra have shapes similar to emissivity spectra, although the mean value of each spectrum is zero. This method is one of several available for extracting emissivity information from thermal-infrared scanner data, such as the normalized emissivity technique described by Realmuto (1990), and the ratio method described by Watson (1992). The alpha-residual method is preferred over the normalized emissivity technique because it allows emissivity variations in all six TIMS channels to be examined and it is less sensitive to noise (Hook and others, 1992; Kealy and Hook, 1993). The alpha-residual method is preferred over the ratio approach because ratios are also very susceptible to noise and are more difficult to relate to laboratory spectra.

The alpha-residual images were studied initially using an unsupervised K-means classification program to help identify spectrally distinct materials within the salt pan (Tou and Gonzalez, 1974). A digital mask was applied to the alpha-residual data to limit the unsupervised classification to only the salt pan. The mask was necessary to avoid undesired classifier attention to the surrounding alluvial fans, which in many areas showed much stronger spectral contrasts than the salt-pan materials. The unsupervised classification was quite effective at identifying spectrally distinctive materials, including at least one spectral class that

was not known from previous field studies using short-wave infrared remote sensing data (Crowley, 1993). However, the classification results did not provide a complete substitute for *a priori* knowledge of the study area, as the important distinction between gypsum/anhydrite and thenardite was not made in the unsupervised classification. Gypsum/anhydrite and thenardite were separated using appropriate input spectra in the next analysis procedure outlined below.

Based on the classification results and general field knowledge of the study area, eleven alpha-residual spectra representing different playa surface materials were identified. These spectra were used as input to a second classification procedure that calculated the vector angle (in 6-channel space) between each input spectrum and each "unknown" spectrum in the TIMS data (Kruse and others, 1993). Smaller vector angle values signify closer spectral similarity. A series of gray scale images was generated (one image for each input spectrum), depicting varying degrees of spectral similarity as a range of digital numbers. The eleven output images were thresholded to better constrain the limits of individual spectral classes; these images then were combined as overlays on a single base image with each spectral class displayed in a different color. The Badwater Basin and the Cottonball Basin data were processed in exactly the same way.

Results

Cottonball Basin:

Plate 1 is a color image showing the distribution of spectra classes in the Cottonball Basin study area. Three of the original eleven input spectra were extracted from different areas of the same surface unit (the halite-rich rough-salt discussed below) and their classification images are combined as a single color overlay (cyan on the composite image). Thus, there are nine color patterns present on Plate 1, although one (salmon) is very sparsely distributed in this part of Death Valley. The same nine color patterns are used on the Badwater Basin image (Plate 2). The color overlays on both plates are superimposed on gray-scale pseudo-temperature images of the salt pan (dark areas are relatively cool; bright areas relatively warm). The pseudo-temperature images are derived from the mean temperature values calculated for each pixel in the alpha-residual procedure (Kealy and Hook, 1993). Areas within the salt pan that are not classified in one of the nine colors generally had low-contrast spectral curves and were not distinguishable spectrally.

Figure 3 shows laboratory and field spectral curves for seven samples representing the main spectral classes in the Cottonball Basin, as well as the corresponding alpha-residual spectral curves extracted from the TIMS data. Spectrum "A" on Figure 3, extracted from an area shown in yellow on Plate 1, represents areas with abundant thenardite (Na-sulfate) in the efflorescent crusts (Table 1). The μ FTIR spectrum for sample A has a distinctive spectral feature that is characteristic of thenardite and which translates to an emissivity minimum in TIMS channels 1 and 2 (also see Fig. 1). The distribution of thenardite around the northern and eastern sides of Cottonball Basin probably reflects the inflow of Na-rich ground and surface waters derived at least in part from the weathering of Furnace Creek formation rocks.

The orange areas on Plate 1 correspond to silty halite-rich crusts without much thenardite and have associated spectral curves that exhibit weak emissivity minima in TIMS channels 3 or 4 due to fine-grained feldspars and clay minerals (Figure 3, spectrum "B"; Table 1). In addition, these spectral curves show a downward slope towards shorter wavelengths, probably due to small amounts of quartz in the surficial sediment. Although the silty halite-rich crusts generally do not contain as much salt as the thenardite-rich crusts, ground-water levels are relatively shallow as indicated by field observations of phreatophytic vegetation and the formation of carbonate cements in many of these areas. (Neither the vegetation nor the cements are directly visible from the imagery).

Spectrum "C" in Figure 3 illustrates the distinctive appearance of pure gypsum/anhydrite (Ca-sulfate), which is indicated by red pixels on Plate 1. Only a few small areas of gypsum/anhydrite are shown on the Cottonball Basin image, although gypsum/anhydrite is present in many field samples as a minor constituent in silty mixtures with quartz, feldspar, or carbonate minerals. Such mixtures typically are very fine-grained and spectrally featureless in the thermal-infrared. Note that even though pure gypsum and anhydrite have distinctive shapes in Figure 1, anhydrite was not distinguished from gypsum in any of the field sample spectra or in the TIMS alpha-residual spectra. This may be related to the fine particle size of the anhydrite, which is formed by the dehydration of gypsum. Furthermore, all anhydrite-bearing field samples were impure and included significant residual amounts of gypsum and/or bassanite (CaSO₄ · 1/2H₂O).

Spectrum "C)" on Figure 3, represents illitic clay and/or muscovite that has been reworked from Furnace Creek Formation sediments and deposited on the Furnace Creek alluvial fan (Plate 1, dark blue pixels). These materials exhibit a emissivity minimum in TIMS channels 3 and 4 (Compare Figs. 1B and 3). A second, weaker, emissivity feature is evident at approximately 11.6 μm in field

sample "D. " The origin of this feature is uncertain, although abundant carbonate minerals in the fan sediments (Table 1) may account for the feature. Spectrum "E" on Figure 3 represents quartz-rich fan gravel overlying silty efflorescent crusts in the northern portion of the image (Plate 1, green pixels). In the southern part of Cottonball Basin, west of the Furnace Creek fan, green pixels mark the presence of quartz-rich marginal mudflats. Although these mudflats occupy a marginal zone that is similar to the silty halite- and thenardite-rich crusts (orange and yellow pixels), the quartz-rich character of the mudflats indicates a different depositional regime. The quartz is mainly derived from quartzite exposures in the adjacent Panamint Range, and depending on which alluvial fan drainage channels are presently active, some marginal areas of the salt pan become quartz-rich, whereas others do not. The green and orange/yellow classification patterns therefore show a distinction between the mudflat environment of primarily detrital sedimentation, and the silty halite/thenardite environment of primarily chemical sedimentation, respectively.

Spectrum "F" on Figure 3 represents halite-rich rough-salt that exhibits low-contrast spectra due to cavity-radiator behavior noted above (Plate 1, cyan pixels). There is considerable subtle spectral variation within the rough-salt unit and many areas are not well mapped even though three spectral classes were combined to represent the unit. This problem stems in part from the use of the vector-angle mapper algorithm, which is relatively insensitive to small variations in spectral shape associated with low-contrast spectra. The rough-salt microtopography occurs in areas of the central salt pan that have near-surface (less than one meter depth), chloride-rich brines, but are slightly elevated, and thus protected against normal seasonal flooding,

The light green areas on Plate 1 consist of halite-rich crusts that also contain the Na-Ca-sulfate mineral glauberite. The spectral shape of these glauberite-

bearing crusts is illustrated by curve "G" in Figure 3. Unlike the spectral curves already discussed, the laboratory spectrum of the glauberite-bearing crusts does not bear a close resemblance to alpha-residual spectra for this very well defined image pattern (Fig. 3). The light green pixels occur in low-lying mudflat areas in the center of the salt pan that are generally the last areas to desiccate completely following a significant rainfall or inflow event. The discrepancy in spectral shape indicates that the spectral characteristics of these areas changed during the seven-month interval between the acquisition of the TIMS data and later field work. A spectral model to explain this behavior is shown in Figure 4. The alpha-residual spectrum (Figure 4, spectrum 1) can be approximated by a 33:66 mixture of muscovite and glauberite-bearing crust (Figure 4, curves 2, 3, and 4). Such mixtures are a possible precursor to more extensive crust development, and may have been common at the time of the TIMS overflight (e.g., assuming that the central mudflat areas had not crusted-over completely). Muscovite is common in samples from the light-green-classified mudflats; however, several other minerals are present (Table 1) and may also contribute to the spectral response.

Figure 5 is a geologic map of Recent saline deposits in the Cottonball Basin area redrawn from Hunt and others (1966). Descriptions of the various map units are given in Table 2.

Even though the geologic map is based on fieldwork performed nearly four decades prior to the present study, the color TIMS image and the map show important similarities. Map areas of the saline facies, carbonate and sulfate zones (map unit "cs") are indicated by the yellow and orange pixels on the image (Plate 1, "A"). As described in Table 2, the lower portions of this unit are subject to flooding by the rise of ground waters during wet periods, a fact that is borne out by the abundant efflorescent salts in the surficial crusts. Orange pixels also map some areas of silty halite (e.g., unit "sh" in the west-central part of the Cottonball

basin) that are transitional in salt content between the saline facies of the sulfate and carbonate zones (unit "cs") and other unclassified silty halite areas. Several map areas of rough-salt and eroded-salt (units "rs" and "os") along the inner margin of unit "cs" are distinguished by cyan pixels on the TIMS image (Plate 1, "F"), although many other rough-salt areas are not classified. Finally, the marsh facies (unit "mf") of Hunt and others (1966) is indicated on the image by darker gray-to-black areas within the salt pan. Such areas are relatively cool due to spring discharge and the evaporation of moisture from the surficial sediments.

Badwater Basin:

The color TIMS image of the Badwater Basin and associated spectral curves from selected areas are shown on Plate 2 and Figure 6, respectively. Figure 7 again shows a geologic map of the Recent saline deposits redrawn from Hunt and others (1966).

The most striking feature of the Badwater Basin image is a fringing zone of magenta- and salmon-colored pixels around the cool (dark) salt flat of the central basin (Plate 2, areas H, I, and J, respectively). These pixels have an unusual emissivity minimum near $10.6\ \mu\text{m}$ (Fig. 6, spectrum H) that evidently is caused by finely-dispersed Na-sulfate impurities in halite. The μFTIR field spectra for these crust areas display the saw-tooth effects of the calibration error, noted earlier (e.g. Fig. 6, spectra H-J); however, the Na-sulfate impurities are detected in XRD analyses that show the presence of a poorly formed mirabilite-like phase (Table 3), and similar spectral features are seen in laboratory spectra of artificial mineral mixtures (Fig. 8, curve B). Note that in preparing the Figure 8 mixture, the component salts were crystallized together from solution, rather than physically mixed as fine-grained powders. The crystallization step was necessary to obtain the correct spectral match. By comparing curves A, B, and C in Figure 8 it can be

seen that the mirabilite-like phase exhibits transmission behavior in the halite medium. The possibility of such behavior in evaporite mixtures was first suggested by Eastes (1989), although he did not reproduce the spectral shapes seen in natural samples by using synthetic mixtures as shown here. In addition, while the example mixture shown in Figure 8 only involves Na_2SO_4 and NaCl , more complex natural mixtures are common. Transmission behavior involving aphthitalite ($(\text{NaK})_3\text{Na}(\text{SO}_4)_2$)-mirabilite-halite mixtures was also simulated by using laboratory mixtures and was observed in some Death Valley samples.

The strength of the $10.6\text{-}\mu\text{m}$ emissivity feature decreases towards the basin center (magenta-to-salmon-to-black transition on Plate 2), either indicating a compositional gradient, or perhaps a moisture gradient with the slightly deeper center of the pan retaining more moisture than the pan margins (Fig. 6, spectra H, I, J). Spectra measured for dry crusts in the central (black) zone seven months after the TIMS overflight do show Na-sulfate features of various intensities (e.g. Fig. 6, spectrum N). This indicates that the $10.6\text{-}\mu\text{m}$ feature in the central part of the salt pan was either masked by moisture, or not yet formed, at the time of the scanner overflight. Notwithstanding this uncertainty, the data show that spectral measurements have the potential to discern Na_2SO_4 -halite compositional variations under dry conditions.

Spectrum K in Figure 6 represents gypsum/anhydrite, which is notably more abundant in the Badwater basin than in the Cottonball basin. Extensive flats of gypsum occur around springs on the western margin of Badwater basin, such as Eagle Borax spring, and near Tule spring (Fig. 2). The gypsum crusts are rejuvenated during periods of high ground-water levels and increased spring discharge; later the crusts desiccate to form bassanite and anhydrite. In contrast to the Cottonball basin, extensive thenardite crusts do not occur in the Badwater basin, although the mineral is locally abundant in mixtures with other minerals

(Crowley, 1993). The greater abundance of gypsum versus thenardite in the Badwater basin reflects the greater concentration of Ca relative to Na in the local inflow waters, and the more calcic rock types from which the waters are derived.

Green pixels in the Badwater Basin (Fig. 6, spectrum L) again represent quartz-rich mudflat areas that generally do not have near-surface ground water and associated efflorescent salts. Dark blue pixels are illite- or muscovite-rich areas (Fig. 6, spectrum M) and orange pixels indicate moderate efflorescent salt development in some areas along the pan margin (Fig. 3, spectrum B). Light green pixels, which in the Cottonball basin indicated glauberite-bearing efflorescent crusts, are relatively uncommon in the Badwater Basin area. Nonetheless, light green pixels do define an unusual crescent-shaped feature on the eastern margin of the Badwater image (Fig. 6, spectrum N). This narrow feature is located in halite-rich crusts immediately to the west of a small alluvial fan. The feature conforms in shape to the fan outline, and represents an area of ground-water inflow along the fan margin that is slower to desiccate than other nearby areas of the salt pan. Based on the spectral similarity of this area to the light green areas in the Cottonball Basin, we believe that silicate-*evaporite* mixtures probably account for the crescent-shaped feature.

Comparing the classified image to the geologic map of the salt pan (Fig. 7) several similarities and some key differences can be noted. One similarity is that the classified image pattern for gypsum/anhydrite (red pixels) corresponds well with the mapped distribution of massive gypsum (map unit "mg"), particularly along the western margin of the salt pan. The extent of the gypsum/anhydrite on the image is somewhat less than that shown on the map because of the modifying effects of other mineral phases (especially silicates) on the gypsum/anhydrite spectral signatures. Orange and yellow pixels on the image again map areas in the carbonate and sulfate zones (map units "cs" and "ci"; Plate 2, area B) and also

include a few areas of silty halite (map unit "sh"). Dark blue pixels representing illite/muscovite are more widely distributed in the Badwater Basin compared to the Cottonball Basin. A strong concentration of these pixels occurs in the upper right portion of the image associated with alluvium derived from the Artist Drive Formation (Plate 2, area M); dark blue pixels are also associated with the eroded salt unit (map unit "es") in the southern (lower) portion of the Badwater image.

An important difference between the geologic map and the TIMS classified image of the Badwater Basin involves the reduced extent of the rough-salt and eroded-salt facies (map units "es" and "rs"; Plate 2, cyan pixels, area O). Boundaries of both units have contracted, in some places by as much as a kilometer, during the 36-year interval between the (ca. 1958) field studies of Hunt and others (1966) and the TIMS overflight. For example, the large triangular region of rough-salt located immediately north of the geologic map centerline is substantially reduced in size on the TIMS image and shows the development of several large semicircular embayments. Previously mapped areas of eroded-salt located to the northwest of the triangular rough-salt region appear black on the recent TIMS image--indicating a smooth, moist, halite/mirabilite crust, rather than an older surface of eroded-salt pinnacles. What these changes may represent in terms of the recent precipitation history of the Death Valley region is considered below.

Discussion

The classified TIMS data depict a number of mineralogical units within the Death Valley salt pan that reflect important aspects of the playa ground-water chemistry, hydrology, and desiccation stage. For example, the Na-rich character of Cottonball Basin inflow waters was indicated by abundant thenardite in many of the efflorescent salt crusts. In contrast, the more Ca-rich inflow waters of the Badwater Basin were marked by the local development of gypsum-dominated crusts. Extensive thenardite or gypsum crusts in both basins represent zones of near-surface ground water that are slightly elevated and, therefore, protected from periodic flooding and immersion. Ground water had less involvement in the formation of some of the other mineralogical units. In particular, the illite-muscovite- and quartz-rich units (dark blue pixels and green pixels) represent areas of surface water runoff and primarily detrital silicate sedimentation. The carbonate zone and silty halite units (orange pixels) appear to be intermediate in terms of efflorescent salt content and ground-water influence.

Several features of the salt pan were discernible to some degree based on textural or moisture variations rather than mineralogical variations. For example, major areas of spring discharge in the salt pan were marked in some cases by mineralogical features (e. g., gypsum crusts) and in other cases by cool pseudo-temperatures related to the evaporation of surface moisture. Similar moisture effects were seen in the Badwater Basin where evaporation enhanced the lowering of surface temperatures over the highly reflective halite crusts. Understanding the TIMS sensitivity to moisture variations is an objective of ongoing field studies.

The halite-rich rough-salt unit produced characteristic low-contrast spectral curves related to cavity radiator behavior and the absence of any minerals exhibiting strong spectral absorption bands. Low spectral contrast can also result from fine particle size (Salisbury and others, 1991), and thus, thermal-infrared spectral

data alone are not sufficient for identifying rough-salt material. The unusual microtopography of the rough-salt does produce a strong radar backscatter signal (Schaber and others, 1976), and the use of radar data in conjunction with thermal-infrared data may afford the best means of mapping rough-salt surfaces.

The Death Valley salt pan undergoes seasonal-to-interannual cycles of wetting and desiccation related to regional precipitation variations. Several remote-sensing observations can be used to estimate desiccation progress, and similar observations should be applicable to playas in other areas. One desiccation indicator is the "crusting over" of mudflats in the central salt pan, which early in a drying cycle exhibit silicate mineral spectra, later followed by spectral mixtures of evaporates with or without silicates. The minerals involved in the spectral mixtures may be different for different playas, but the desiccation behavior of the central mudflat subenvironment should be consistent. Another type of indicator is the development of halite-rich spectral mixtures with mirabilite or other highly soluble phases that do not form until late in the desiccation cycle. Again, although mirabilite mixtures were common in Death Valley, other minerals may be important in playas with different brine compositions. Finally, there is the observation noted above that the evaporation of surface moisture can reduce the temperature of salt crusts. The shrinkage of areas affected by this evaporative cooling may provide a remote-sensing indicator of desiccation progress during a wetting/drying cycle.

The desiccation phenomena described above occur in response to relatively short-term moisture fluctuations. Other features within a playa have different susceptibilities to regional moisture changes. For example, more permanent features, such as the rough-salt and eroded-salt unit boundaries, are likely to reflect moisture variations on longer time scales.

In recent decades several floods within the Death Valley salt pan have sharply reduced the areas of the rough-salt and eroded-salt map units of Hunt and

others (1966). The floods were caused by heavy inflow from the Amargosa River, including major episodes in 1969 and 1983-84 when the central portion of Badwater Basin was immersed to depths exceeding one meter (Hunt, 1975; U. S. Geological Survey, 1984; 1985). The 1969 and 1983-84 floods raised water levels enough to destroy the characteristic microtopography along the rough-salt and eroded-salt unit margins. Some of these changes were noted by Hunt (1975) and the development of the changes through time is clearly seen on aerial photographs (Plate 3). That the 1983-84 flooding was especially unusual is shown by the large affected area of rough salt and the lack of subsequent regeneration of the rough- salt and eroded-salt units (compare Figure 7 and Plates 2 and 3). Other available photographic images and climatic data suggest that changes in the Badwater Basin salt deposits of the magnitude seen in 1983-84 had not occurred for at least the preceding 72 years (unpublished data--Death Valley National Park photographic archives; Death Valley National Park precipitation records) It therefore seems likely that the time scale for such destructive flooding events, and the time scale for the salt units to regenerate, is on the order of decades, or longer.

Moisture variations on decadal-to-centennial timescales are occurring in Death Valley, Figure 9 shows a three-year running average of rainfall measured at the Furnace Creek Ranch from 1913-1993. Even in these smoothed data there is marked interannual variability; however, it is evident that the past two and one-half decades have been distinctly wetter on average than the five preceding decades. This overall pattern of increased precipitation has been observed throughout the Great Basin, as shown by tree-ring data from northeastern Nevada (Nichols, 1989), and by the expansion of the Great Salt Lake from an historic minimum level in 1963 to an historic maximum in 1986 (Hassibe and Keck, 1991).

Are the shifting salt unit boundaries a response to decadal-scale climatic changes or simply an effect of rare weather conditions? To answer this question will require a more complete review of regional climatological data, perhaps combined with evaporation and runoff modeling of the Death Valley hydrologic basin. Investigation of thermoluminescent and other dating techniques that might be used to determine the ages of salt units is also needed. If playa observations are to provide a basis for climate monitoring, many playas will need to be examined and changes in their salt units related to available climatic and other data. Our understanding of playa evaporite crusts and their response to climatic change remains limited. However, it is clear that playas offer unusual opportunities for studying climatic effects on hydrology and other environmental aspects of arid basins,

Summary and Conclusions

A single flight line of Thermal Infrared Multispectral Scanner (TIMS) data was acquired in April, 1994, over Death Valley, California, and used to study the evaporite mineralogy of the salt pan. The data were calibrated, corrected for atmospheric effects using the MODTRAN radiative transfer model, and processed to extract emissivity information by using the method of alpha-residuals. An unsupervised K-means classification algorithm was used initially to aid in identifying spectrally distinct materials. A supervised classification based on a vector-angle measure of spectral similarity was then applied to map nine spectral classes representing various surface materials. These classes were displayed in different colors on a pseudo-temperature image derived as part of the alpha-residual procedure.

The map patterns of the spectral classes were investigated by using laboratory and field spectroscopic measurements, and by X-ray powder diffraction studies of field samples. The spectral differences between units were found to reflect a number of factors including evaporite and silicate mineralogy, moisture variations, and mixture effects. Natural halite-mirabilite crusts showed unusual spectral features resulting from the transmission of energy through small grains of mirabilite suspended in a matrix of halite. These spectral features were measured in the field and recreated by laboratory experiments in which artificial mixtures of NaCl and Na_2SO_4 were crystallized together from solution.

Evaporite mineral distributions show important relations to the inflow water chemistry and hydrology of the Death Valley salt pan. Large areas of thonardite (sodium sulfate) were limited to the northern Cottonball Basin, an area where inflow waters are rich in sodium. Extensive gypsum (calcium sulfate) crusts occurred in the Badwater Basin, particularly near springs characterized by more calcic ground waters. Abundant evaporite minerals generally marked areas where

ground water is periodically near the surface, and thus, able to replenish the salt crusts via capillary evaporation. Detrital silicate minerals predominated in other areas where shallow ground water was absent. There were close similarities between the classified TIMS imagery and the units defined on an existing geologic map of the salt pan. Although the geologic map was largely based on geomorphic features and sedimentary facies in the shallow subsurface, a number of map units had some mineralogical or textural expression that was discernible with the TIMS data. As thermal-infrared data become more widely available, it will be necessary to better understand relations between surface spectral properties and subsurface materials and processes.

Different mineralogical features of playas respond to regional moisture variations on different time scales. For example, salt crusts formed on low-lying floodplains reflect seasonal-to-interannual wetting/desiccation cycles. Other features of playa evaporite crusts may reflect longer-term climatic changes. In particular, the shrinkage of rough- and eroded- salt units in Death Valley due to recent episodes of flooding may represent a response to increased regional precipitation spanning several decades. Understanding playa responses to climate change will require a synthesis of mineralogical information and climatological data from many different playa settings.

Observations like those of the present study require sensors which have at least four to six channels in the 8-12 μm wavelength region, a capability that is currently available only on airborne systems. A major step forward in thermal-infrared remote-sensing will occur with the launch of the Earth Observing System AM-1 platform in 1998. The platform will include the Advanced Spaceborne Thermal Emission and Reflectance Radiometer (ASTER), which will provide multispectral-thermal imagery, albeit at lower spatial resolution (90 m pixels) than the TIMS data used here (20 m pixels). With ASTER data it should be possible to

detect and monitor important changes in playas and to study related climatic and environmental variables on a global scale.

Acknowledgments

A number of reviewers took the time to study and offer constructive criticism of this manuscript. For this we are grateful to A. R. Gillespie, D. H. Knepper, F. D. Palluconi, J. W. Salisbury, and J. P. Smoot. Special thanks are also due to the National Park Service staff of Death Valley National Park for their continuing cooperation and assistance. This study was supported by the U. S. Geological Survey Mineral Assessment Techniques Program and by the National Aeronautics and Space Administration Geology Program.

References

Barker, C. E., and Barker, J. M., A re-evaluation of the origin and diagenesis of borate deposits, Death Valley region, California, *in* Borates: Economic Geology and Production, edited by J. M. Barker and S. J. Lefond, Amer. Inst. of Mining, Metallurg., and Petrol. Engineers., New York, 101-135, 1985.

Barker, J. M., and Wilson, J. L., Borate deposits in the Death Valley region, *in* Guidebook: Las Vegas to Death Valley and Return, Nevada Bureau of Mines and Geology Report 26, Mackay School of Mines, University of Nevada, Reno, 23-32, 1975.

Berk, A., Bernstein, L. S., and Robertson, D. C., MODTRAN: A moderate resolution for LOWTRAN 7, Report GL-TR-89-01 22, Geophysical Laboratory, Air Force Systems Command, Hanscom Air Force Base, Massachusetts, 38 P., 1989.

Crowley, J. K., Visible and near-infrared (0.4-2.5 μm) reflectance spectra of playa evaporite minerals, *J. Geophys. Res.*, 96, 16,231-16,240, 1991.

Crowley, J. K., Mapping playa evaporite minerals with AVIRIS data: A first report from Death Valley, California, Remote Sens. Environ., 44, 337-356, 1993.

Eastes, J. W., Spectral properties of halite-rich mineral mixtures: Implications for middle infrared remote sensing of highly saline environments, *Remote Sens. Environ.*, 27, 289-304, 1989.

Eugster, H. P., Geochemistry of evaporitic lacustrine deposits, *in* Ann. Rev. of Earth and Planet. Sci., edited by F. A. Donath, 8, 35-63, 1980.

Eugster, H. P., and Hardie, L. A., Saline lakes, in Lakes--Chemistry, Geology, Physics, edited by A. Lerman, Springer-Verlag, New York, 237-293, 1978.

Farmer, V. C., The Infrared Spectra of Minerals, Mineralogical Society Monograph 4, London, 539 p., 1974.

Hassibe, H. R., and Keck, W. G., The Great Salt Lake, U. S. Geological Survey, General Interest Publications, U. S. Government Printing Office, 24 p., 1991.

Hook, S. J., Gabell, A. R., Green, A. A., and Kealy, P. S., A comparison of techniques for extracting emissivity information from thermal infrared data for geologic studies, *Remote Sens. Environ.*, 42, 123-135, 1992.

Hook, S. J., and Kahle, A. B., The micro Fourier Transform Interferometer (μ FTIR) - A new field spectrometer for validation of infrared data, *Remote Sens. of Environ.*, (in press).

Hunt, C. B., Death Valley--Geology, Ecology, Archaeology, University of California Press, Berkeley, 234 p., 1975.

Hunt, C. B., and Mabey, D. R., Stratigraphy and structure, Death Valley, California, U. S. Geological Survey Prof. Paper 494-A, Washington, D. C., 162 p., 1966.

Hunt, C. B., Robinson, T. W., Bowles, W. A., and Washburn, A. L., Hydrologic basin, Death Valley, California, U. S. Geological Survey Prof. Paper 494-B, Washington, D. C., 138 p., 1966.

Hunt, G. R., Electromagnetic radiation: The communication link in remote sensing, in Remote Sensing in Geology, edited by B. S. Siegal and A.R. Gillespie John Wiley and Sons, New York, 5-45, 1980.

Hunt, G. R., and Salisbury, J. W., Visible and near-infrared spectra of minerals and rocks: II. Carbonates, Modern Geol., 2, 23-30, 1971.

Hunt, G. R., Salisbury, J. W., and Lenhoff, C. J., Visible and near-infrared spectra of minerals and rocks: IV. Sulphides and sulphates, Modern Geol., 3, 1-14, 1971.

Hunt, G. R., Salisbury, J. W., and Lenhoff, C. J., Visible and near-infrared spectra of minerals and rocks: V. Halides, phosphates, arsenates, vanadates, and berates, Modern Geol., 3, 121-132, 1972.

Kealy, P. S., and Hook, S. J., Separating temperature and emissivity in thermal infrared multispectral scanner data: Implications for recoloring land surface temperatures, Geoscience and Remote Sensing, 31, 1155-1164, 1993.

Kruse, F. A., Lefkoff, A. B., Boardman, J. W., Heidebrecht, K. B., Shapiro, A. T., Barloon, P. J., and Goetz, A. F. H., The Spectral Image processing System (SIPS)-- Interactive visualization and analysis of imaging spectrometer data, Remote Sens. Environ., 44, 145-163, 1993.

McAllister, J. F., Geology of the Furnace Creek borate area, Death Valley, Inyo County, California: Map Sheet 14, California Division of Mines and Geology, San Francisco, 9 p., 1970.

McAllister, J. F., Columnar section of the main part of the Furnace Creek Formation of Pliocene (Clarendonian and Hemphillian) age across Twenty Mule Team Canyon, Furnace Creek borate area, Death Valley, California, U. S. Geological Survey Open-File Report 76-261, 1 p., 1976.

Nichols, W. D., Reconstructed drought history, north-central Great Basin: 1601-1982, in Aspects of Climate Variability in the Pacific and the Western Americas, edited by David H. Peterson, Geophysical Monograph 55, American Geophysical Union, Washington, D.C., 61-67, 1989.

Palluconi, F. D., and Meeks, G. R., Thermal infrared multispectral scanner (TIMS): An investigators guide to TIMS data, JPL Pub. 85-32, Jet Propulsion Laboratory, Pasadena, 1985.

Realmuto, V. J., Separating the effects of temperature and emissivity: Emissivity spectrum normalization, in Proceedings of the Second Thermal Infrared Multispectral Scanner (TIMS) Workshop, edited by E. Abbott, JPL Pub. 90-55, 31-35, 1990.

Realmuto, V. J., Hajek, P., Sinha, M. P., and T. G. Chrien, The 1994 laboratory calibration of TIMS, in Summaries of the Fifth Annual JPL Airborne Earth Science Workshop, Jan. 23-26, 1995, 2, JPL pub. 95-1, 25-28, 1995a.

Realmuto, V. J., Hook, S. J., and J. van den Bosch, The 1994 TIMS airborne calibration experiment: Castaic Lake, CA., *in* Summaries of the Fifth Annual JPL Airborne Earth Science Workshop, Jan. 23-26, 1995, 2, JPL Pub. 95-1, 29-32, 1995b.

Reeves, C. C., Jr., Economic significance of playa lake deposits, International Association of Sedimentologists, Spec. Pub. 2, 279-290, 1978.

Ross, S. D., Sulphates and other Oxy-anions of Group VI, *in* The Infrared Spectra of Minerals, edited by V. C. Farmer, Mineralogical Society Monograph 4, London, 423-444, 1974.

Salisbury, J. W., Walter, L. S., Verge, N., D'Aria, O. M., Infrared (2.1-25 μm) Spectra of Minerals, The Johns Hopkins University Press, Baltimore, 267 p., 1991.

Salisbury, J. W., and D'Aria, D. M., Emissivity of terrestrial materials in the 8-14 μm atmospheric window, Remote Sens. Environ., 42, 83-106., 1992.

Salisbury, J. W., Wald, A., and D'Aria, D. M., Thermal-infrared remote sensing and Kirchhoff's Law: I Laboratory measurements, J. of Geophys. Res., 99, 11897-11911, 1994.

Schaber, G. G., Berlin, G. L., Brown, W. E., Jr., Variations in surface roughness within Death Valley, California: Geologic evaluation of 25-cm-wavelength radar images, Geol. Soc. of Amer. Bull., 87, 29-41, 1976.

Smith, G. I., Borate deposits in the United States: Dissimilar in form, similar in geologic setting, in Borates: Economic Geology and Production, edited by J. M. Barker and S. J. Lefond, Amer. Inst. of Mining., Metalurg., and Petrol. Engineers., New York, 37-51, 1985.

Smith, G. I., Friedman, I., and McLaughlin, R. J., Studies of Quaternary saline lakes--III. Mineral, chemical, and isotopic evidence of salt solution and crystallization processes in Owens Lake, California, 1967-1971, Geochim. Cosmochim. Acts, 51, 811-827, 1987.

Smoot, J. P., and Lowenstein, T. K., Depositional environments of non-marine evaporates, in Evaporates, Petroleum and Mineral Resources, edited by J. L. Melvin, Developments in Sedimentology No. 50., Elsevier, Amsterdam, 189-347, 1991.

Tou, J. T., and Gonzalez, R. C., Pattern Recognition Principles, Applied Mathematics and Computation, No. 7, Addison-Wesley Publishing Co., Reading, Massachusetts, 94-104, 1974.

U. S. Geological Survey, Water Resources Data, Volume I, California, Water year 1983, Water Resource Report CA-83-1, Amargosa River gauge at Tecopa, P. 33, 1984.

U. S. Geological Survey, National Water Summary, 1984, Water Supply paPer 2275, 467 p., 1985.

Vine, J. D., Nonpegmatite lithium resource potential, in Lithium Resources and Requirements by the Year 2000, edited by J. D. Vine, U. S. Geological Survey Prof. Paper 1005, 54-58, 1976.

Watson, K., Spectral ratio method for measuring emissivity, Remote Sens. Environ. 42, 113-116, 1992.

Figure Captions

Figure 1A. Laboratory directional-hemispherical reflectance spectra converted to emissivity using Kirchhoff's law ($Emission = 1 - Reflectance$) for a number of common evaporite minerals. The same spectra are plotted on the right after convolution to the six TIMS filter functions. Spectra are offset on the vertical axis for clarity; bracket indicates an emissivity interval of 0.1 except for the ulexite and trona spectra, where the indicated interval is 0.05. Y intercept values are 0.99, 0.99, 0.93, 1.0, 1.0, 0.98, 0.98, and 0.97 (top to bottom).

Figure 1 B. Laboratory directional-hemispherical reflectance spectra converted to emissivity using Kirchhoff's law ($E = 1 - R$) for a number of common silicate minerals. The same spectra are plotted on the right after convolution to the six TIMS filter functions. Spectra are offset on the vertical axis for clarity; bracket indicates an emissivity interval of 0.1 except for quartz, where the indicated interval is 0.2. Y intercept values are 0.92, 0.99, 0.98, 0.99, 0.99, and 0.99 (top to bottom).

Figure 2. Generalized geologic map of study area modified from Hunt and Mabey (1966). Abbreviated geographic names: EBS = Eagle Borax Spring; TS = Tule Spring; FCR = Furnace Creek Ranch. Centerline of TIMS imagery also shown.

Figure 3. (left) Emissivity spectra of field samples representing various image spectral classes. Spectra are offset on the vertical axis for clarity; bracket indicates an emissivity interval of 0.05 except for "E," where the indicated interval is 0.15. Y intercept values are 0.98, 0.96, 0.98, 0.90, 0.92, 0.97, and 0.95 (top to bottom). The majority of spectra were recorded in the field using the $\mu FTIR$ field emission spectrometer. In the cases of spectra "C," "E," and "G," laboratory

directional-hemispherical reflectance spectra of field samples were converted to emissivity by using Kirchhoff's law ($E = 1 - R$). (middle) Spectra from the left column after convolution to the six TIMS filter functions. (right) Alpha-residual spectra for single pixels extracted from the TIMS data. Areas used for the extraction are labeled "A"- "G" on Plate 1, with the exception of area "6," which is on Plate 2. Surficial units represented by these spectra are: "A, " thenardite-rich crusts in saline facies of sulfate zone; "B, " silty halite, smooth facies, and carbonate zone, silty facies; "C, " gypsum crusts; "D, " illite/muscovite-rich alluvial deposits; "E, " quartz-rich fan gravels and mudflats; "F, " massive halite and silty halite, rough facies; "G, " mixed silicate and evaporite mineral crusts on floodplains. Unit descriptions are modified from Hunt and others (1966).

Figure 4. Spectral model of mixed silicate and evaporite mineral crusts on floodplains of the central Cottonball Basin (Plate 1, unit "G"). Alpha-residual spectra for this unit, represented by the upper curve, can be modeled as a spectral mixture of muscovite and glauberite-bearing crust. Such mixtures may have been common at the time of the TIMS overflight assuming that the central mudflat areas had not completely crusted-over. Although muscovite is an important constituent of the floodplain sediments, other silicates, including smectitic clay, feldspar, and quartz, are also present and may be involved in the spectral response.

Figure 5. Geologic map of Recent saline deposits in Cottonball Basin (modified from Hunt and others, 1966). Abbreviations of map units: mf = marsh facies; cs = saline facies of sulfate and carbonate zones; sh = silty halite, smooth facies; sf = sand facies of carbonate zone; rs = silty halite and massive halite, rough facies; es = eroded halite; fp = floodplain deposits. Descriptions of each map unit are provided in Table 2.

Figure 6. (left) Emissivity spectra of field samples representing various image spectral classes. Spectra are offset on the vertical axis for clarity; bracket indicates an emissivity interval of 0.05 except for "N", where the indicated interval is 0.1. Y intercept values are 0.84, 0.95, 0.96, 0.98, 0.96, 0.98, and 0.75 (top to bottom). The majority of spectra were recorded in the field using the μ FTIR field emission spectrometer. In the case of samples "L" and "N," the laboratory hemispherical reflectance was converted to emissivity by using Kirchhoff's law ($E = 1 - R$). (middle) Spectra from the left column after convolution to the six TIMS filter functions. (right) Alpha-residual spectra for single pixels extracted from the TIMS data. Areas used for the extraction are labeled "H"- "N" on Plate 2. Surficial units represented by these spectra are: "H," "I," and "J", smooth halite-rich crusts on floodplains; "K," gypsum crusts; "L," quartz-rich alluvial deposits; "M," illite/muscovite-rich alluvial deposits; "N," mixed silicate and evaporite mineral crusts on floodplains. Unit descriptions are modified from Hunt and others (1966). Note that the μ FTIR spectra for samples with low emissivity in the 10.0-12.5 μ m wavelength region (Spectra "I"-"J") show the saw-tooth effects of a calibration error (see text). A better comparison can be made between convolved laboratory spectra and alpha-residual spectra for sample areas that exhibit the 10.6 μ m emissivity minimum (compare curve "N," middle column, with curves "H" and "I," right column).

Figure 7. Geologic map of Recent saline deposits in Badwater Basin (modified from Hunt and others, 1966). Abbreviations of map units: mf = marsh facies; cs = saline facies of sulfate and carbonate zones; ci = silt facies of the carbonate zone; mg = massive gypsum; rs = silty halite and massive halite, rough facies; es = eroded halite; sh = silty halite, smooth facies; sf = sand facies of carbonate zone; fp = floodplain deposits; ds = dune sand. Unit descriptions are in Table 2.

Figure 8. Experimental data to explain the origin of emissivity minima near $10.6\ \mu\text{m}$ (reflectance maxima) in halite-rich crusts of the central Badwater Basin and elsewhere. Upper panel--Spectral curve "C" is a laboratory spectrum of a natural sample which shows a deep reflectance feature near $9.0\ \mu\text{m}$ and a strong increase in reflectance to $10.6\ \mu\text{m}$. Such features are not caused by halite, which lacks spectral features in the $8.0\text{-}12.5\ \mu\text{m}$ wavelength region. The natural sample spectrum resembles the spectrum of an artificial salt crust produced by crystallizing an aqueous solution of NaCl and Na_2SO_4 in a 9:1 mixture (curve "B"). Curve "A" is a transmission spectrum of mirabilite that has been resealed for comparison to the two reflectance spectra "B" and "C." The $9.0\ \mu\text{m}$ feature seen in the reflectance spectra, as well as the weaker feature near $10.0\ \mu\text{m}$, appear to be caused by transmission behavior of mirabilite. A mirabilite-like phase is consistently found in X-ray powder diffraction analyses of halite-rich crusts that exhibit this spectral behavior (Table 3). Lower panel--The natural sample reflectance (Upper panel, curve "C") was transformed to emissivity by using Kirchhoff's Law ($E = 1 - R$), yielding curve "D." This spectrum was convolved to the TIMS filter functions (curve "E") for comparison to a representative alpha-residual spectrum extracted from the TIMS data set (curve "F").

Figure 9. Precipitation data for the Furnace Creek Ranch, 1913-93. Data are presented as a three-year running average to suppress year-to-year variations and to more clearly show long-term trends. Precipitation totals for the most recent two and one-half decades are well above the average for the period of record. Other climatic data sets point to increased regional precipitation throughout the Great Basin for the same time period.

Plate Captions

Plate 1. Pseudo-temperature image of the Cottonball Basin study area with color overlays showing the distribution of various spectral classes. Labels A-G indicate areas used to extract the single-pixel alpha-residual spectra shown in Figure 3.

Note that the "B" extraction site is on Plate 2. Surficial units represented by various image colors are: "A, " yellow pixels--thenardite-rich crusts in saline facies of sulfate zone; Orange pixels--silty halite, smooth facies, and carbonate zone, silty facies; "C, " red pixels--gypsum crusts; "D, " dark-blue pixels--illite/muscovite-rich alluvial deposits; "E, " green pixels--quartz-rich fan gravels and mudflats; "F, " cyan pixels--massive halite and silty halite, rough facies; "G, " light-green pixels--mixed silicate and evaporite mineral crusts on floodplains. Unit descriptions are modified from Hunt and others (1966).

Plate 2. Pseudo-temperature image of the Badwater Basin study area with color overlays showing the distribution of various spectral classes. Labels H-N indicate areas used to extract the single-pixel alpha-residual spectra shown in Figure 6; the spectrum for site "B" is shown in Figure 3. Surficial units represented by various image colors are: Yellow pixels--thenardite-rich crusts in saline facies of sulfate zone; "B," orange pixels--silty halite, smooth facies, and carbonate zone, silty facies; "H, " "I," and "J", magenta, salmon, and black pixels--smooth halite-rich crusts on floodplains; "K, " red pixels--gypsum crusts; "L, " green pixels--quartz-rich alluvial deposits; "M, " dark-blue pixels--illite/muscovite-rich alluvial deposits; "N, " light-green pixels--mixed silicate and evaporite mineral crusts on floodplains. Cyan pixels--massive halite and silty halite, rough facies. Unit descriptions are modified from Hunt and others (1966). "O" indicates a rough-salt area that has changed since the geologic mapping by Hunt and others (1966).

Plate 3. Aerial photographs of the central Badwater Basin showing changes in the halite-rich rough-salt unit of Hunt and others (1966) occurring from 1948-1989. Note the dark boot-shaped feature seen in the upper half of the 1948 and 1976 images and its markedly reduced size in the 1989 image. Erosion of the unit resulted from flooding episodes in 1969 and 1983-84.

Table 1. X-ray powder diffraction analyses for reference minerals and field samples.

Minerals listed in order of abundance. Minor components indicated by (m).

Sample	XRD Composition
--------	-----------------

Figure 1A- Evaporite Reference Minerals

Thenardite	thenardite (Saline Valley, Calif.)
Gypsum	gypsum (Mesquite Playa, Calif.)
Anhydrite	synthetic sample (R. A. Robie, USGS)
Hexahydrite	synthetic sample (J. K. Crowley, USGS)
Bloedite	bloedite (Soda Lake, Calif.)
Glauberite	glauberite (NMNH R591 4) ¹
Ulexite	ulexite (Boron, Calif.)
Trona	trona (Green River Fm, Wyo.)

Figure 1B- Silicate Reference Minerals

Quartz	quartz (Death Valley, Calif.)
Albite	albite (HS-66 ² ; Amelia, Virg.)
Muscovite	muscovite (Mt. Turner, Australia)
Illite	illite (Marblehead, Wis.)
Kaolinite	kaolinite (Mesa Alta, New Mex., CM S-93)
Montmorillonite	montmorillonite (Apache Co., Ariz.)

Figure 3- Field Samples, Cottonball Basin

A	Halite, thenardite, dolomite, quartz, muscovite
B	Albite, halite, muscovite, quartz, dolomite (m), calcite (m)
C	Gypsum, anhydrite
D	Dolomite, calcite, quartz, albite, illite/muscovite
E	Quartz
F	Halite, thenardite (m)
G	Halite, glauberite, mirabilite (m)

Figure 4- Silicate-Evaporite Mixtures

Muscovite	muscovite (Mt. Turner, Australia)
Glauberite Crust (evaporite fraction)	Halite, glauberite, mirabilite (m)
Glauberite Crust (detrital fraction)	Quartz, muscovite, albite, smectite, dolomite (m), kaolin (m)

Figure 6- Field Samples, Badwater Basin

H	Halite, mirabilite (m)
I	Halite, mirabilite (m)
J	Halite, mirabilite (m)
K	Anhydrite, bassanite, gypsum
L	Halite, quartz, dolomite, calcite, gypsum, muscovite (m)
M	Halite, quartz, albite, calcite, illite/muscovite
N	Halite, mirabilite (m)

¹ Sample obtained from the Smithsonian Institution National Museum of Natural History

² Sample obtained from Hunt and Salisbury mineral collection, USGS, Denver, Colo.

³ Clay Mineral Society standard sample CMS-9

Table 2. Description of Recent saline deposits modified from Hunt and others (1966)

mf -- Marsh deposits	Ground generally wet. Sulfate salts with halite, except carbonate salts in marsh areas on east side of Cottonball Basin.
cs -- Saline facies of carbonate and sulfate zones	Surface layer is brown silt 15-45 cm thick containing sulfate salts. Underlain by irregular slabby halite 30-100 cm thick. Low parts are subject to flooding by rise of water table during protracted wet periods.
ci -- Silt facies of carbonate zone	Silty playa beds impregnated with carbonate salts and capped by crust of halite in blister forms 2-8 cm thick. Sulfates occur as small nodules in a layer 1 cm thick about 8 cm below surface. Ground is generally damp and frequently wet from a combination of surface runoff and shallow ground water.
sf -- Sand facies of carbonate zone	Carbonate salts impregnating sandy playa deposits, commonly with a caliche-like layer of sulfate salts 8-15 cm below surface. Ground elevated and subject to flooding only by local runoff.
mg -- Massive gypsum	60-200 cm thick, capped by anhydrite or bassonite. A surface is a silty layer containing various salts and elastic mineral, probably eolian. Elevated and protected against flooding.
rs -- Rough salt	Includes silty rock salt, rough facies, and massive rock salt unit of Hunt and others (1966). Silty rock salt is capped by a silt layer 2-5 cm thick containing sulfate salts. Surfaces are rough. Elevated and protected against flooding.

es -- Eroded salt	Silty rock salt 2-40 cm thick, overlies silt. Reworked from other chloride zone deposits. Subject to occasional flooding.
sh -- Silty halite	Silty rock salt, smooth facies, of Hunt and others (1966). Surface layer is silt 5-50 cm thick containing sulfate and borate salts. Thins panward. Underlain by smooth layer of halite 5-50 cm thick that thickens panward. Subject to some flooding by runoff on this surface.
fp -- Flood plains	Sand and silt. Extensive salt efflorescence and thin salt crusts. Seasonally flooded.
ds -- Dune sand	Active dunes. Surface rarely flooded. Ground water shallow but low in dissolved solids.

Table 3. X-ray diffraction data for halite-rich sample containing mirabilite(?) impurities.

Sample		Mineral assignment ¹	Mirabilite (111-647) ²	
dÅ	Intensity		dÅ	Intensity
7.56	12	M	7.55	1
--	--	--	6.11	17
5.54	41	M	5.49	100
5.34	23	M	5.32	25
5.23	14	M	5.17	5
4.90	12	M	4.88	20
--	--	--	4.77	45
--	--	--	4.32	20
4.09	7	A	--	--
3.94	17	M	3.95	15
3.86	12	M	3.83	40
--	--	--	3.58	17
--	--	--	3.40	17
3.25	62	H, M	3.26	60
--	--	--	3.21	75
--	--	--	3.11	60
3.06	7	M	3.06	3
2.94	18	M, A	2.94	13
--	--	--	2.85	20
2.82	100+	H, M	2.80	30
--	--	--	2.74	13
--	--	--	2.69	11
--	--	--	2.57	13
--	--	--	2.52	35

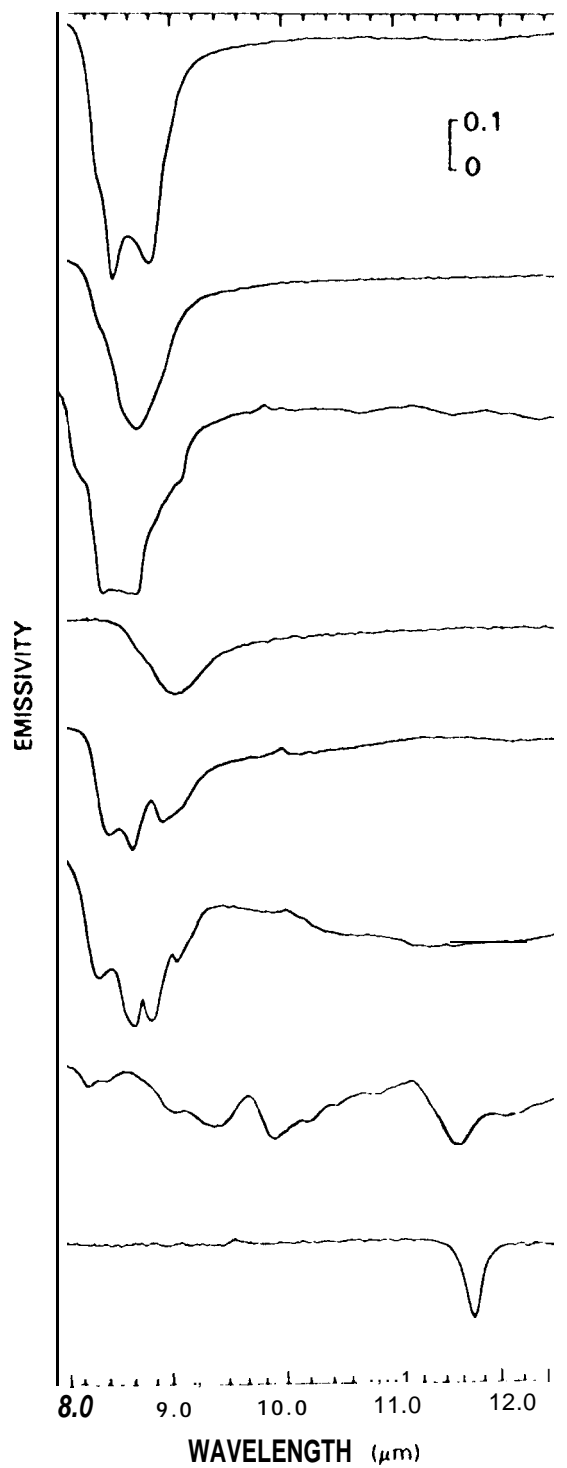
--	--	--	2,49	20
--	--	--	2,44	25
.				
.				
1.99	100+	H	--	--

¹ H = Halite, A = Aphthitalite, M = Mirabilite

² Minor peaks are omitted from the reference pattern unless a sample peak was observed at that position.

LABORATORY SPECTRA

TIMS CONVOLVED



THENARDITE

GYPSUM

ANHYDRITE

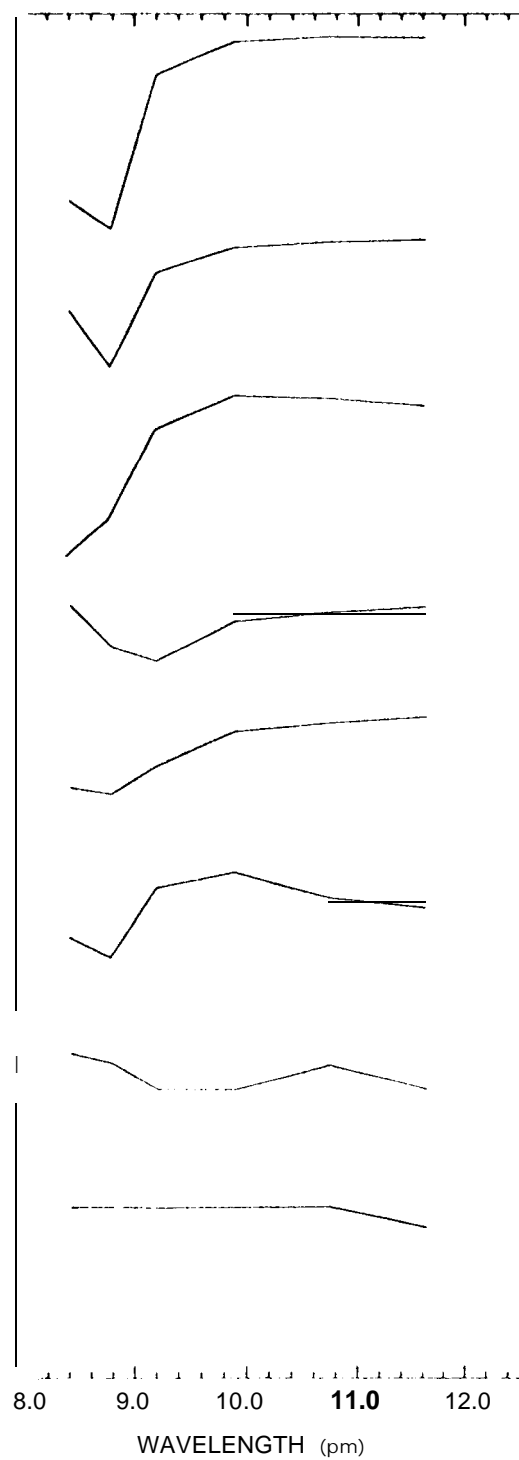
HEXAHYDRITE

BLOEDITE

GLAUBERITE

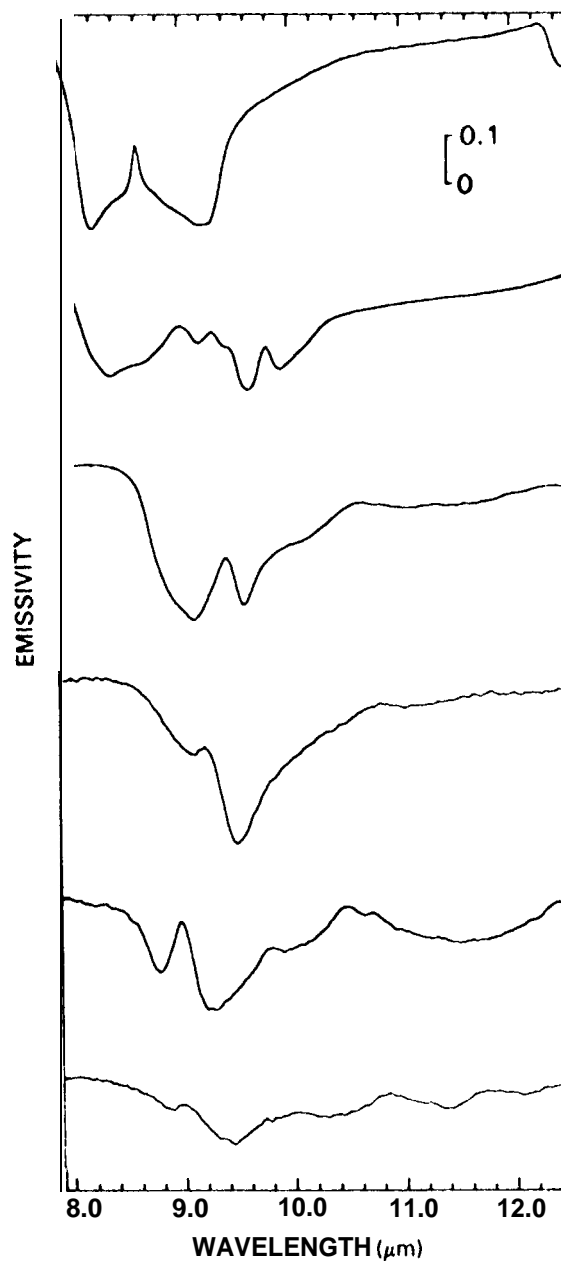
ULEXITE

TRONA



LABORATORY SPECTRA

TIMS CONVOLVED



QUARTZ

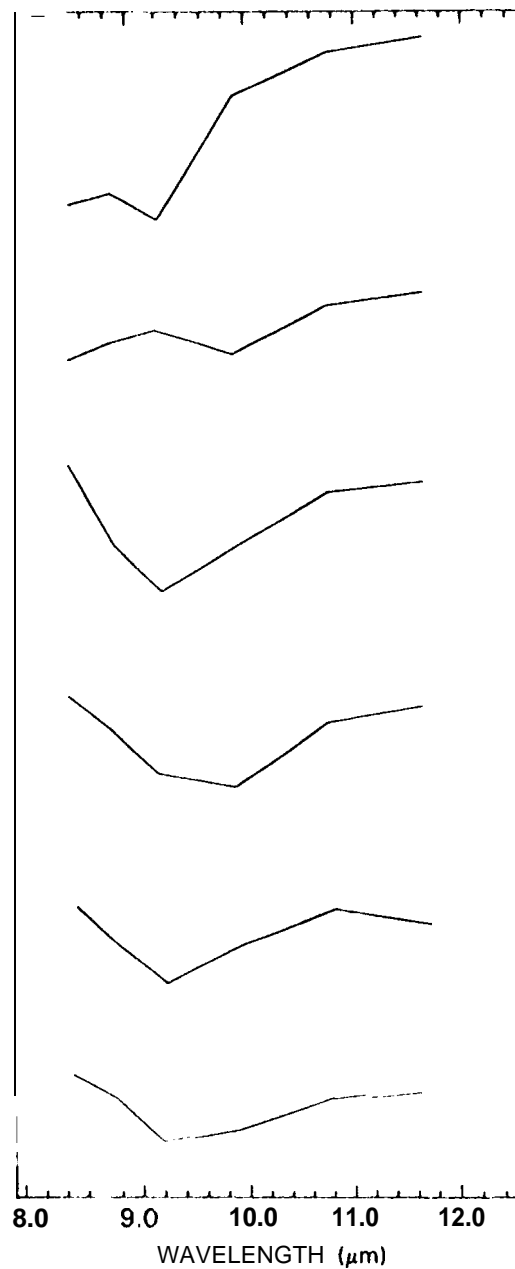
ALBITE

MUSCOVITE

ILLITE

KAOLINITE

MON MORILLONITE



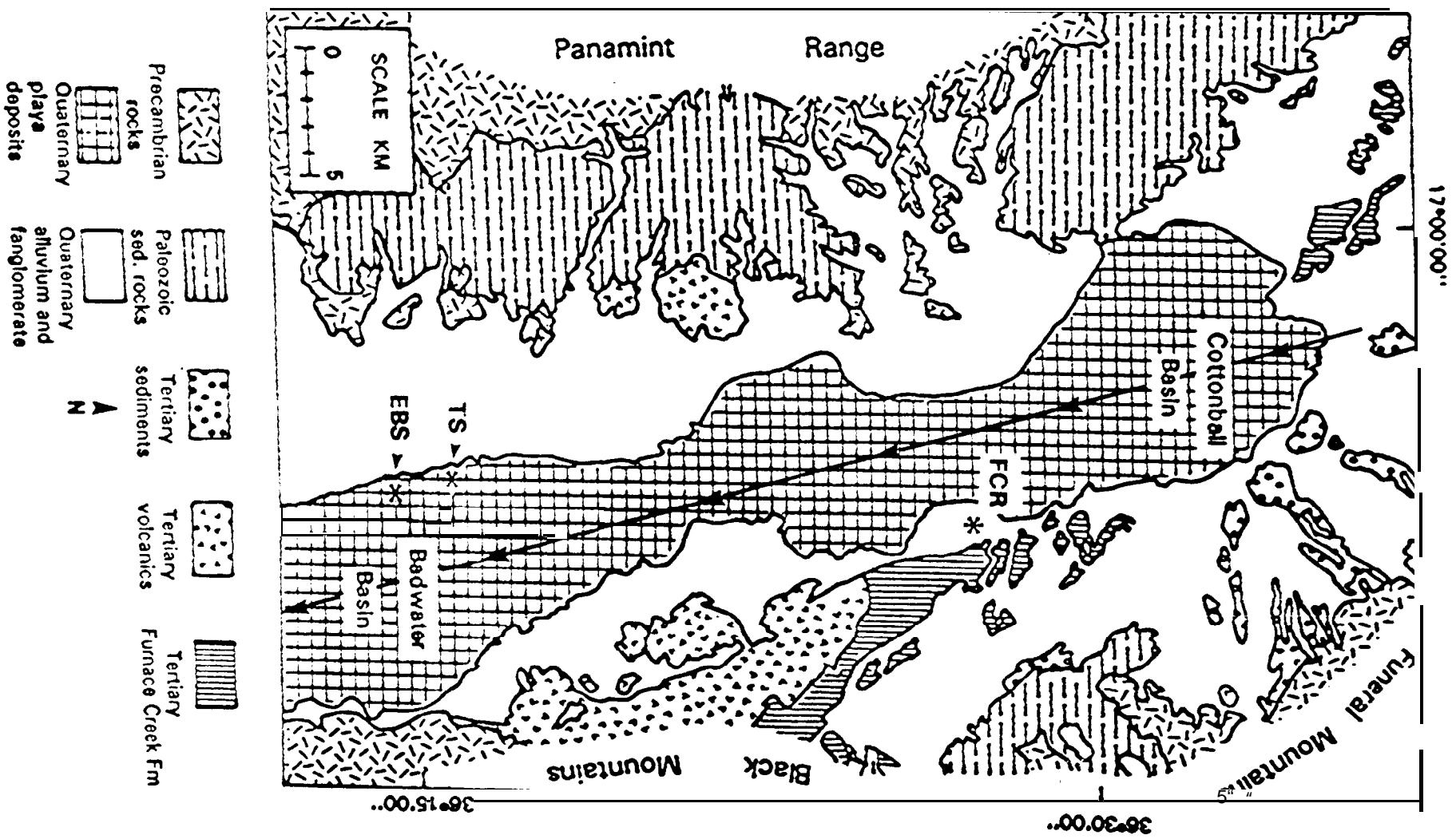
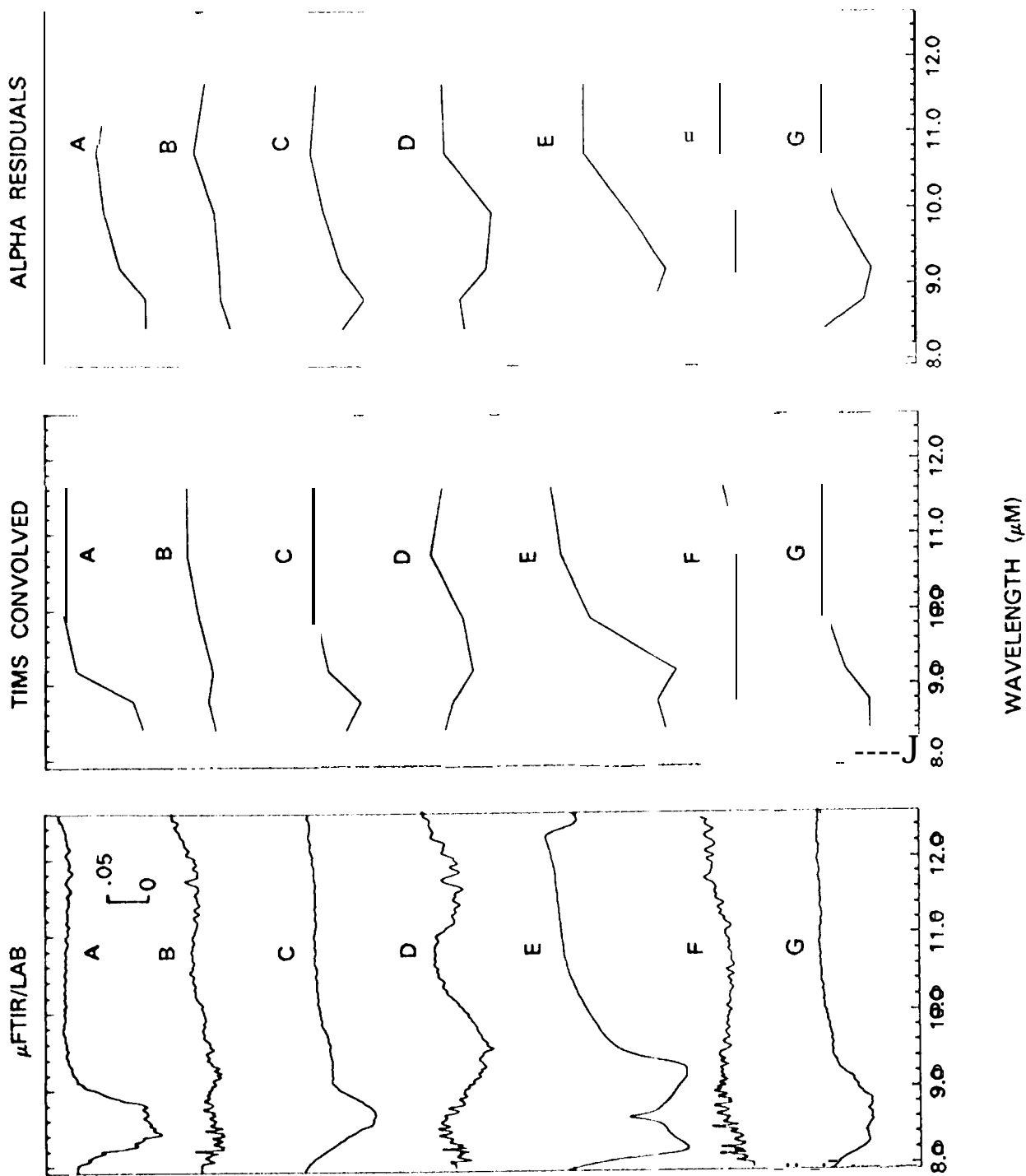


Fig. 2



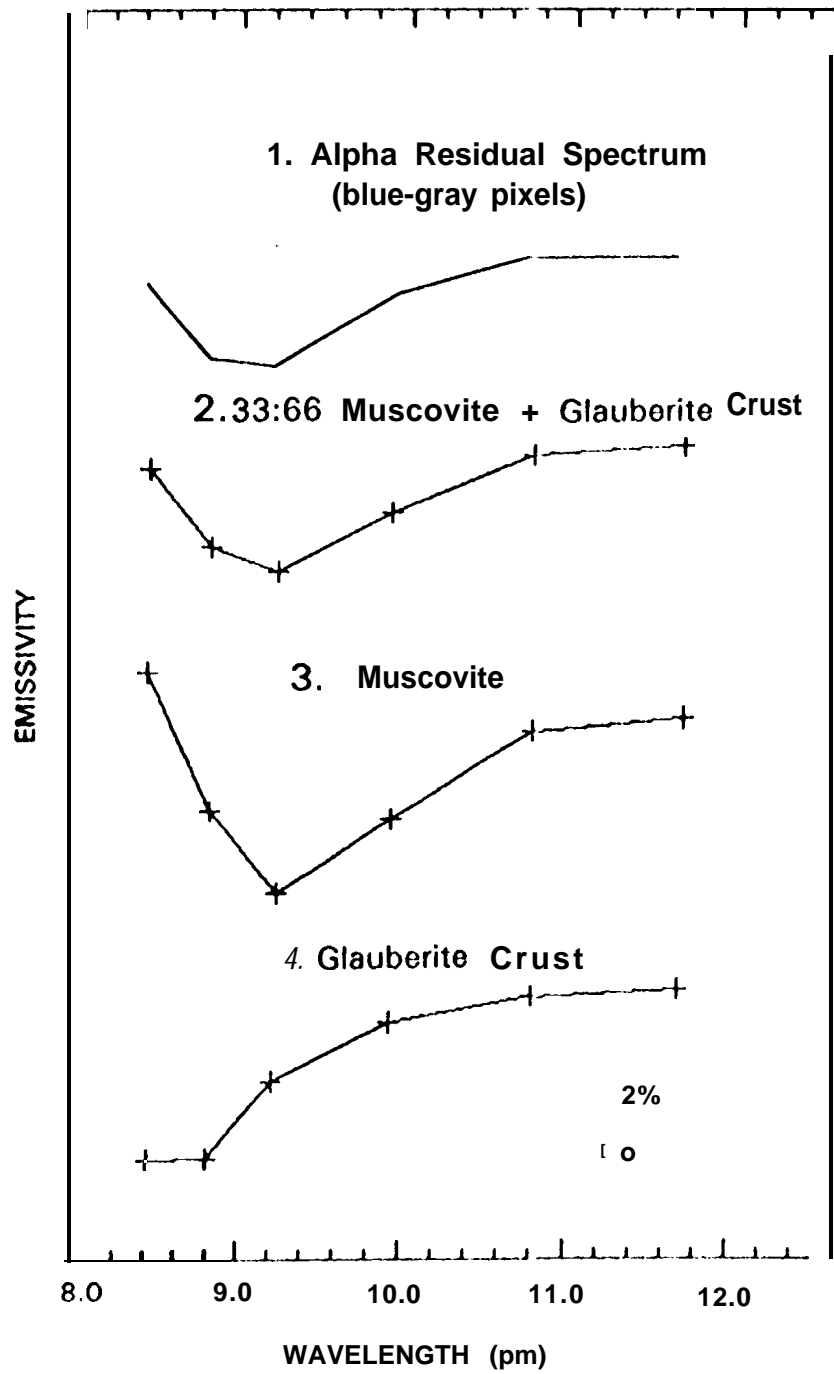
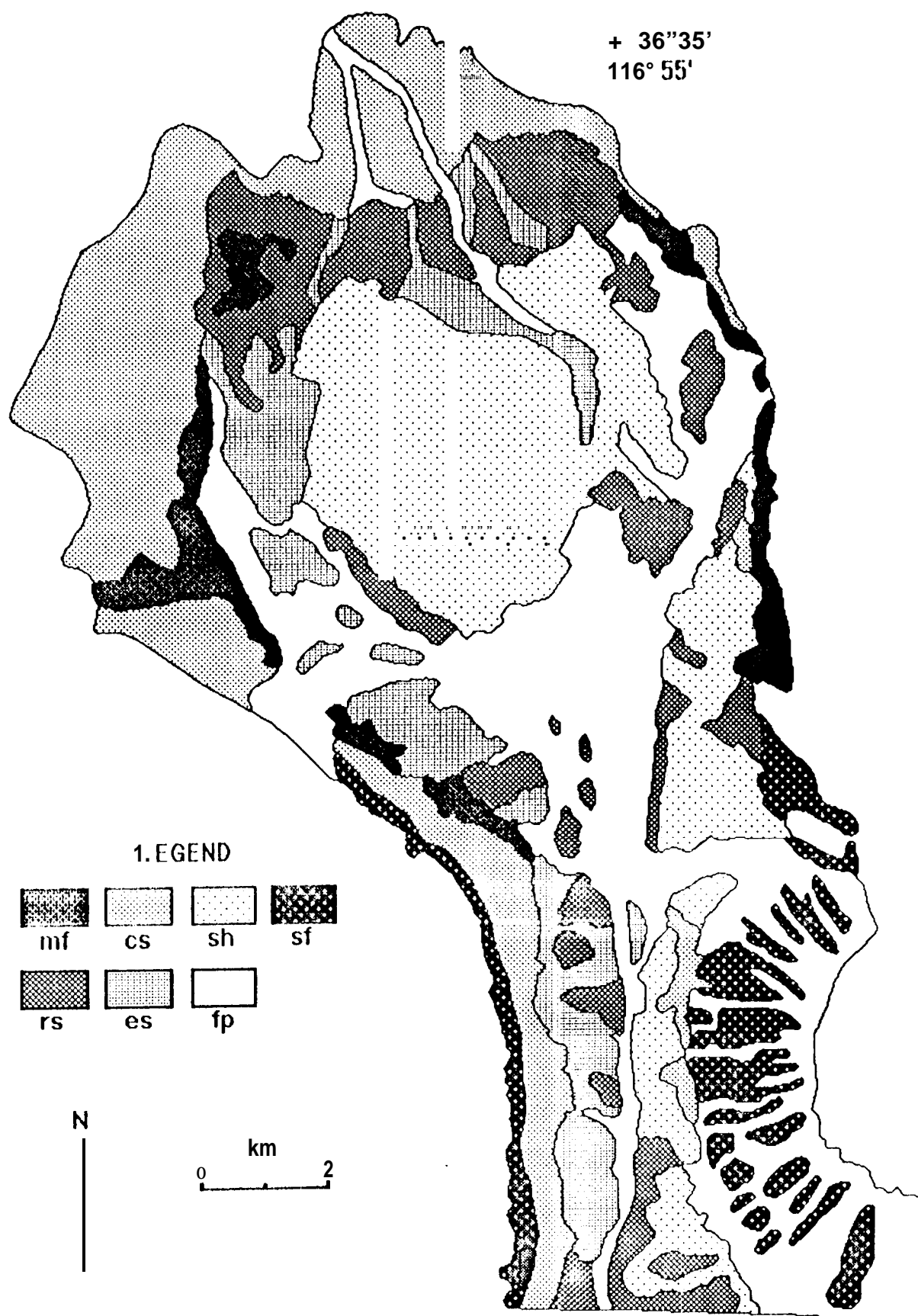


Fig. 5



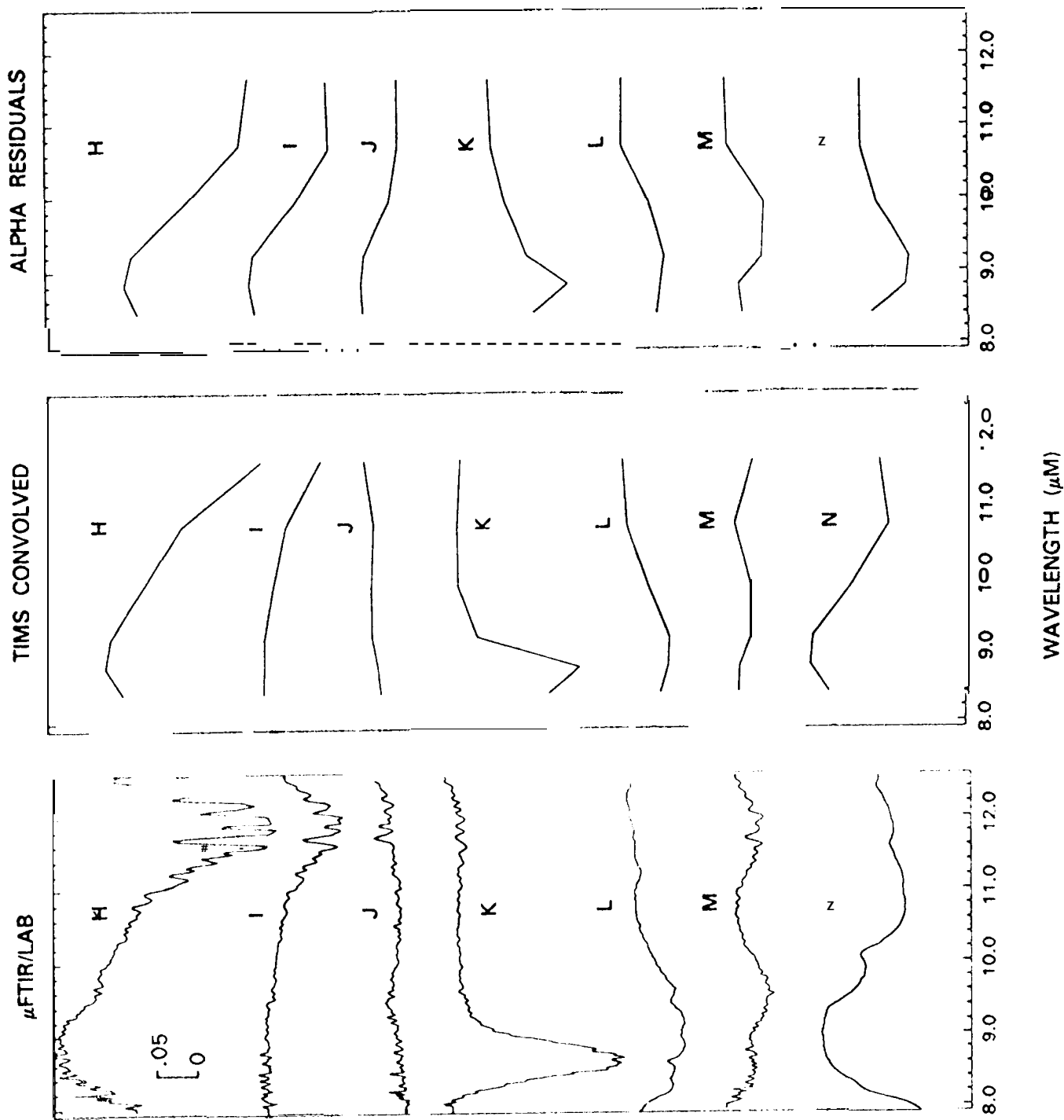
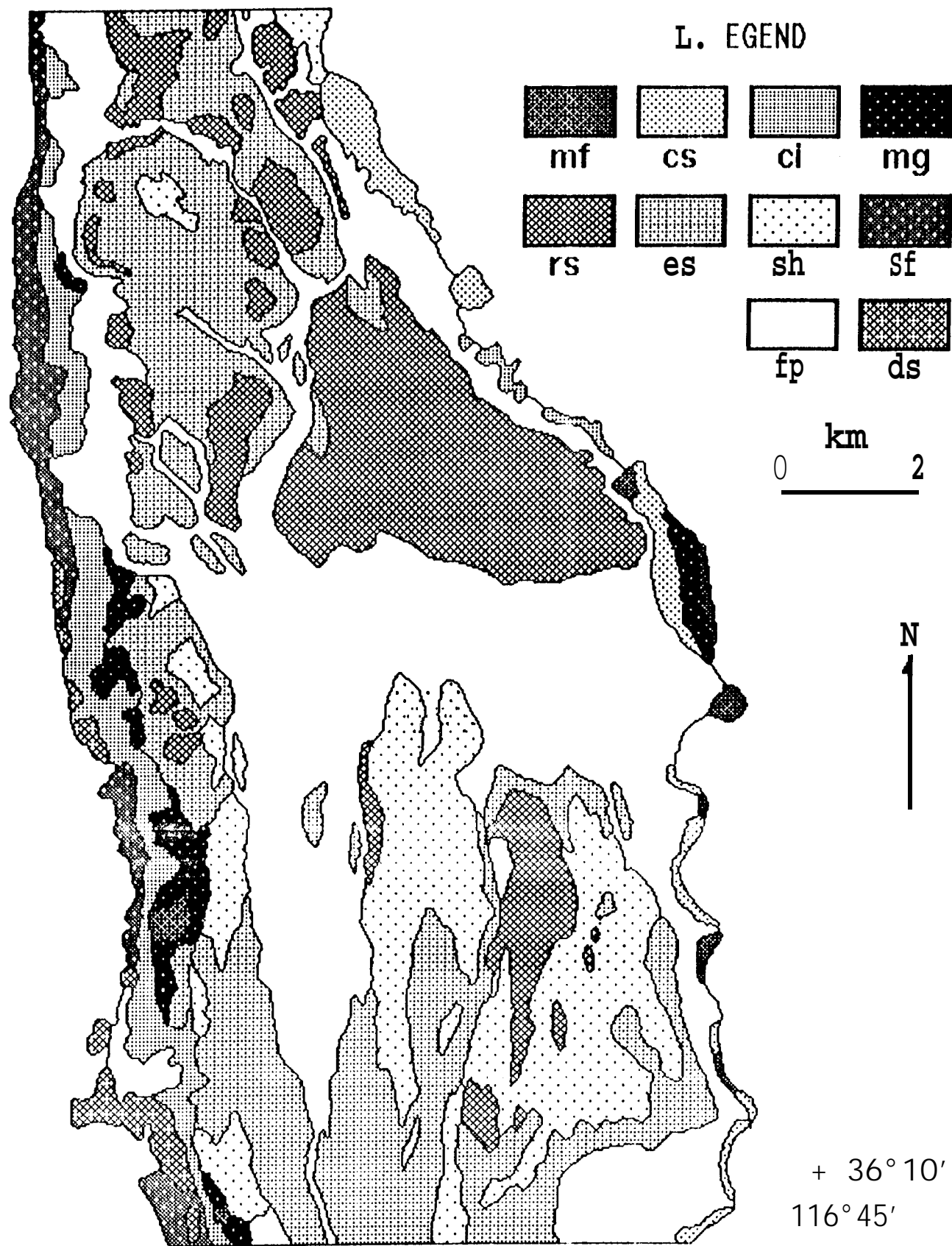
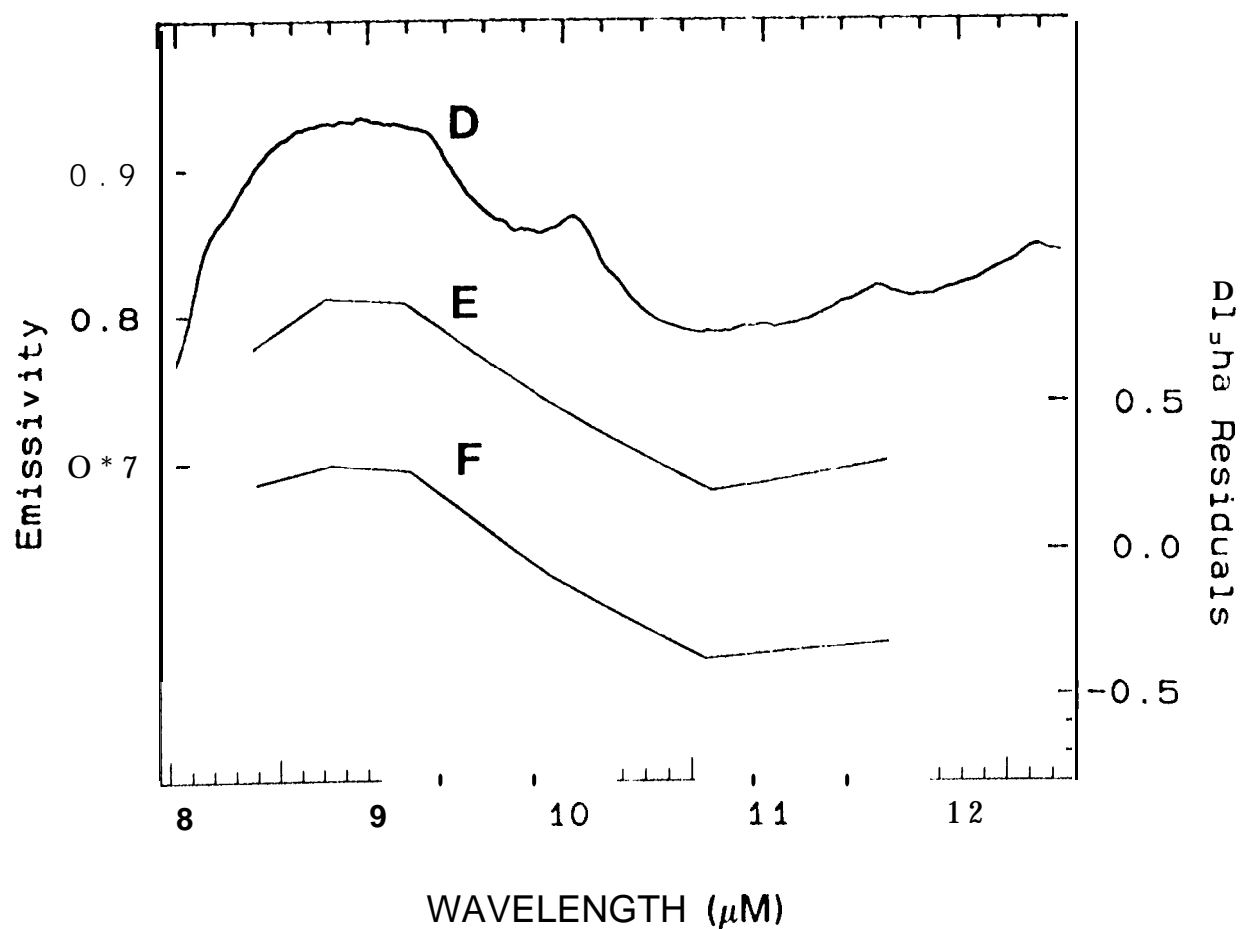
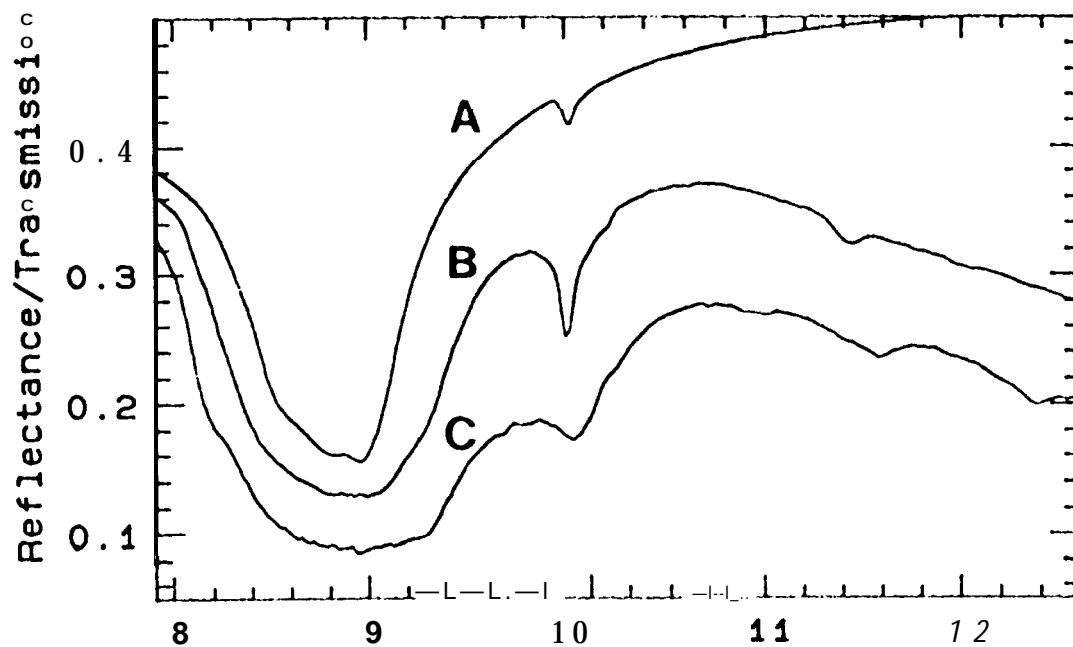


Fig 6

Hy 1





DEATH VALLEY, CALIFORNIA
3-YEAR AVERAGE Precipitation 1913-89

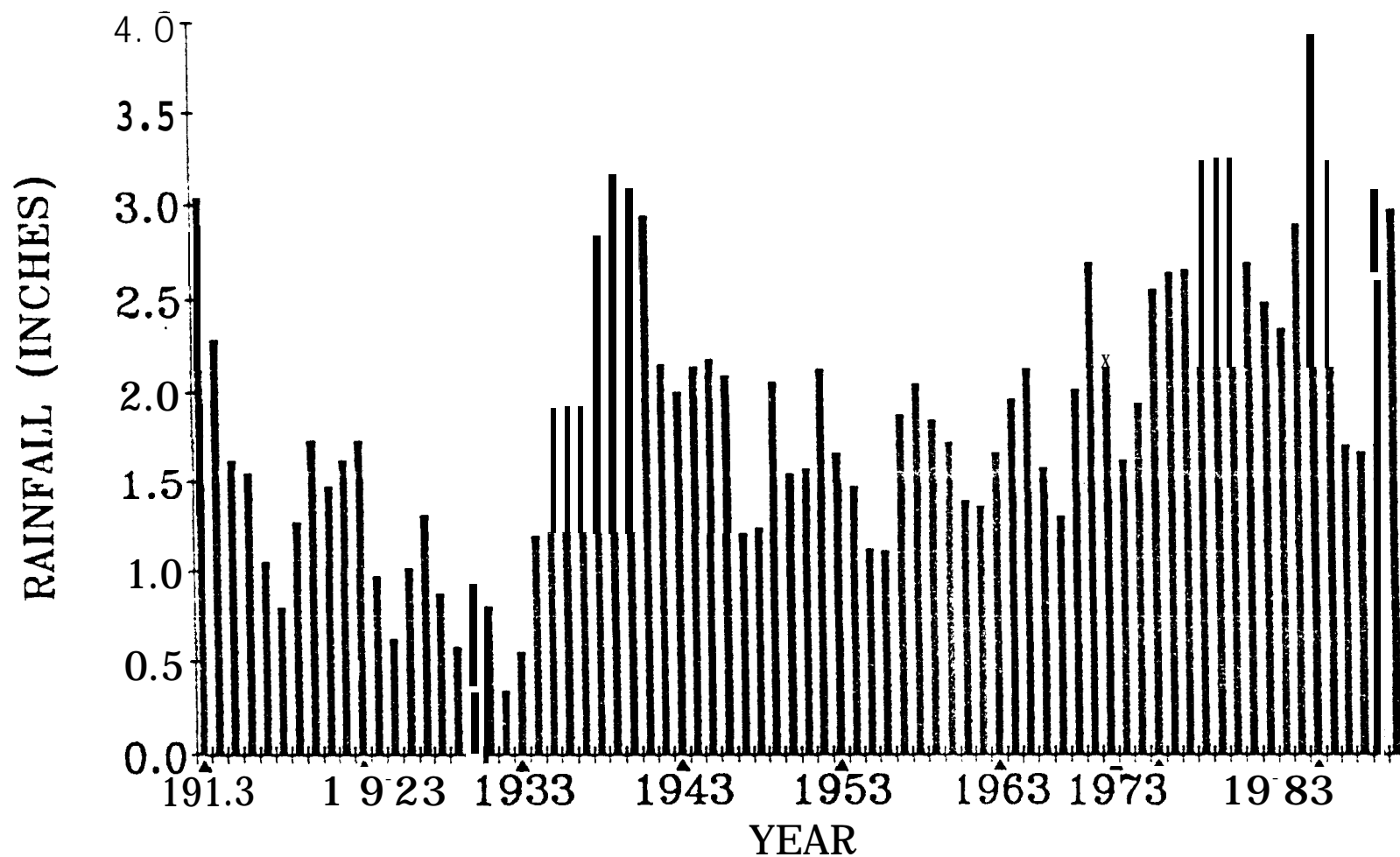
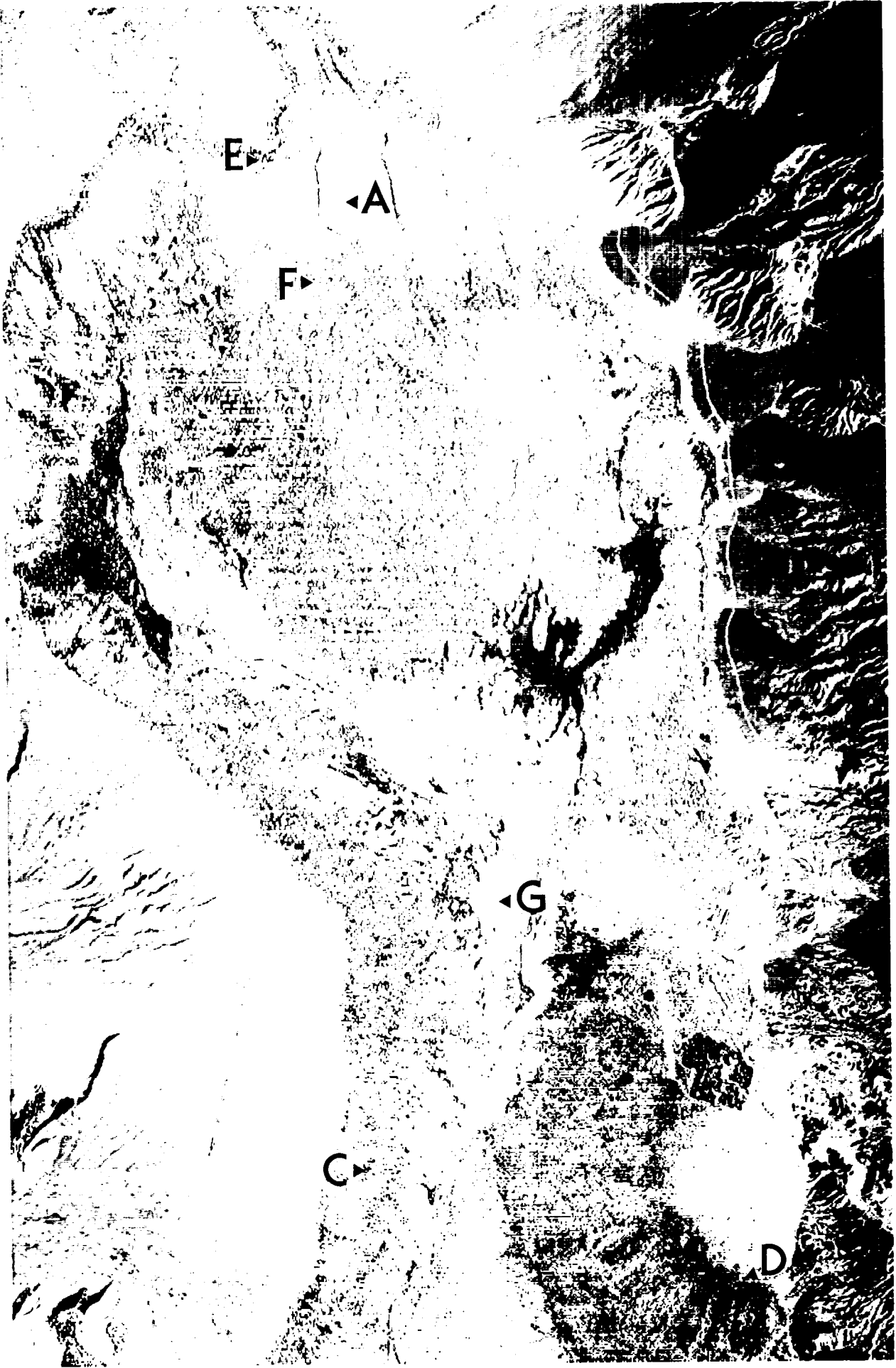
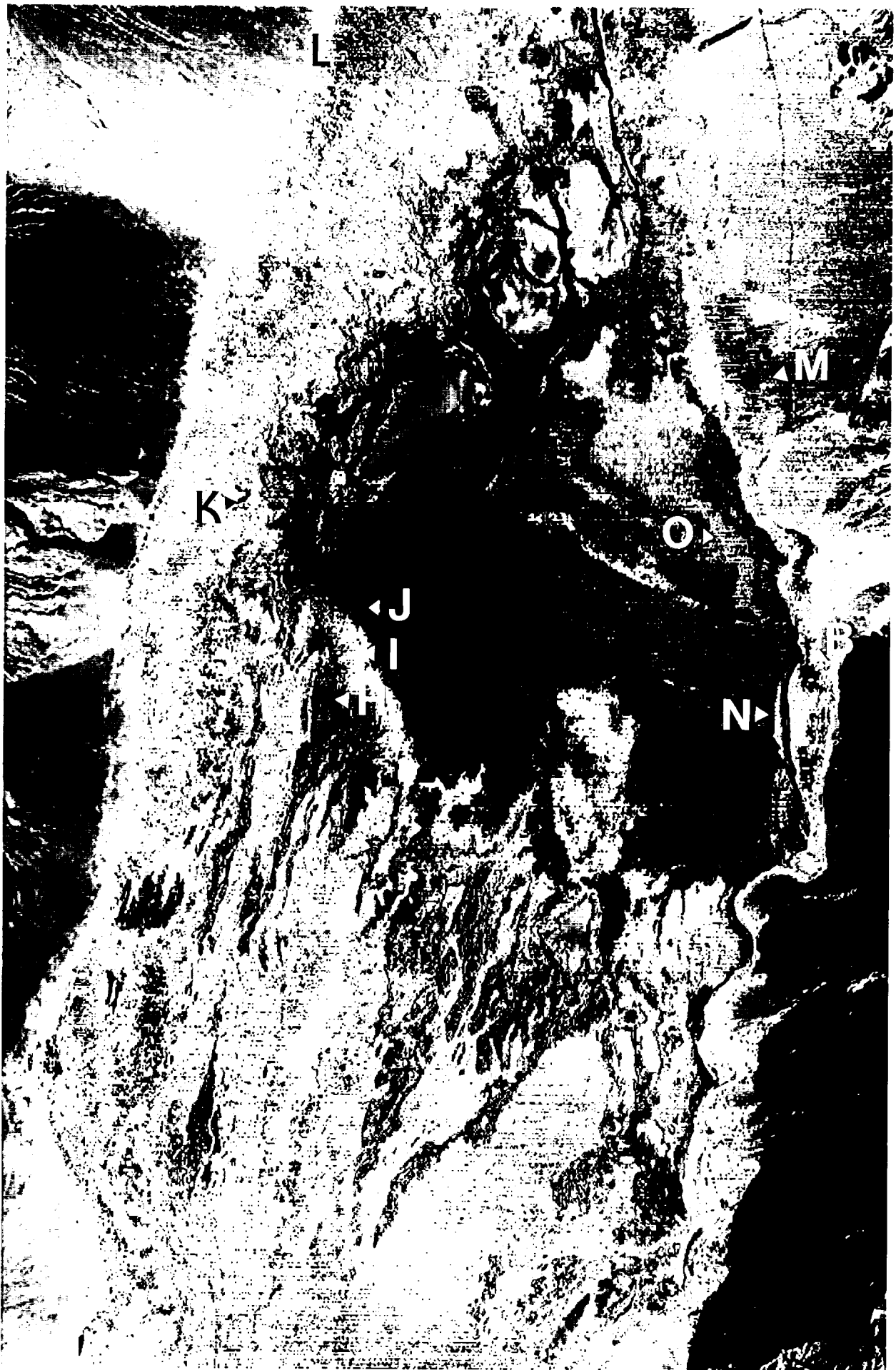


Fig. 9



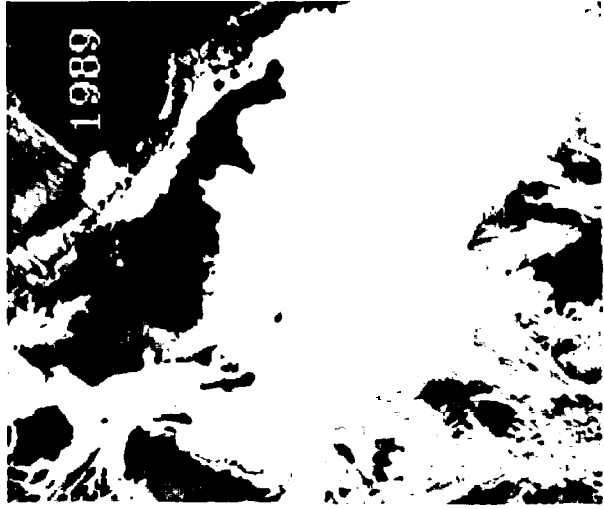




1948



1976



1989